Band Dispersion in Serpentine Channels of Microfluidic Electrokinetic Separation Systems

by

Ryan S. Magargle

A thesis submitted in partial fulfillment of the requirements for the degree of

Master of Science

in

Electrical and Computer Engineering

May 18, 2003

Department of Electrical and Computer Engineering
Carnegie Mellon University
Pittsburgh, Pennsylvania, USA

Advisors: Dr. James F. Hoburg and Dr. Tamal Mukherjee

Table of Contents

Introduction

On-chip capillary electrophoresis was first developed in the early 1990's [1] and remains an important separation technique for microfluidic systems today. The motivation to shrink separation systems comes from their increased portability, reduced consumption of expensive reagents, and more feasible parallel analysis of separations. Since the separation efficiency increases with the separation length, serpentine channels have become a preferred design topology because of their high channel density. However, introducing turns into the separation channel creates additional sources of variance from the new electric field structure and geometric path length differences.

These additional sources of dispersion have been previously modeled in [2,3,4,5]. The problem with each of these models is that they are based on the assumption of a linear electric field structure in a single-turn, which excludes many higher-order effects. This work shows a new model of the high Peclet variance for entire serpentine channels using the full structure of the electric fields described by complete solutions to Laplace's equation. This model is based on closed-form algebraic expressions for rapid computation and possible use in gradient-based optimization. It is a functional model type, as described in [6], for serpentine channels of an arbitrary number of turns. The new variance description can be used in a component-based model for lab-on-a-chip systems that consist of an injector, serpentine separation channel, and detector, which is a common separation system topology [7].

1. Background

Electrophoresis is the method used for species transport in separation microchannels for this work. There are four main types of electrokinetic phenomena [8,9,10]: Electrophoresis, electroosmosis, sedimentation potential, and streaming potential. The first two are the main types of transport used in electrokinetic separation systems. This section will briefly introduce double layer theory, and then discuss its application to electroosmosis and electrophoresis in order to form the basic set of equations governing the dynamics of the separation systems in this report.

1.1 The Double Layer

In general, when two phases form an interface (such as the liquid buffer and solid insulating wall), a spontaneous separation of charge occurs. The separation of the charge into two components at the dual-phase interface is what gives the double layer its name. As stated by Hunter [10], there are several reasons for such a separation:

1. differences between the two phases' affinity for electrons,
2. differences between the two phases' affinity for ions,
3. ionization of surface groups, and
4. entrapment of fixed charge in one phase.

The specific details of each of the four processes above are quite involved and Hunter describes the specifics in [10]. These four processes are responsible for the creation of a surface charge on the channel walls and the formation of the double layer between the wall and the buffer. This surface charge causes dissociated ions or other charge in the buffer of opposite polarity to accumulate in a double layer near the wall, as seen in figure 1. In general, there are ions of both types of charge in an electrolyte buffer solution. However, the concentration of counterions (ions shielding the surface charge) is generally much greater than that of co-ions (ions of charge similar to the wall's surface). The positive and negative charges in the mobile half of the double layer (the diffuse portion that exists within the liquid buffer) are described by Boltzmann's equation [10]:

$$n_{\pm} = n_{\pm}^{o} \exp\left(\frac{-z_i q_e \Phi}{kT}\right), \qquad (1)$$

where $n_{\pm}$ is the local positive or negative ion concentration, $n_{\pm}^{o}$ is the ion concentration in the bulk, z_i is the valency of ion i, q_e is the charge of an electron, Φ is the electric potential that goes to zero as $n_{\pm}$ goes to $n_{\pm}^{o}$, k is Boltzmann's constant, and T is the temperature. When Φ is positive as with a positively charged surface, $n_{+} < n_{+}^{o}$, i.e., positive ions are repelled from the double layer, and $n_{-} > n_{-}^{o}$ which means negative ions are attracted to the double layer.

1.2 Electroosmosis

For electroosmosis, when an electric field is applied axially along the channel, the high concentration of counterions in the double layer feels a force and begins to move. This concentration of counterions dominates any opposing drag of co-ions. The net effect drags all subsequent layers adjacent to the double layer and this slip-boundary condition (which is a valid analogy when the double layer is small compared to the channel) quickly forms a plug flow in the channel [9]. Since the buffer is the system component that moves, this type of transport does not require that the species itself be charged.

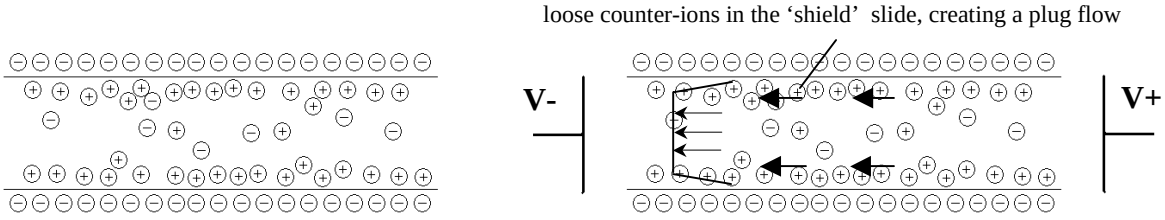

Figure 1 – (a) Double layer formed on channel walls in electroosmotic separation. (b) Motion of the double layer and resulting plug flow.

The double layer is not a well-defined boundary. The composing ions are subject to thermal excitations and other free particle interactions, which cause them to diffuse and create a diffusion boundary around the charged surface. One way to characterize the double layer is to apply Poison's equation, $\nabla^2 \Phi = \rho / \varepsilon$, within the layer and solve for the potential. There will be a certain potential a small distance away from the charged surface where the particles in the double layer will be able to flow

past the surface. At this shear surface, the potential is called the zeta potential, ζ, [8,9,10]. At a certain distance beyond the zeta potential point, there will be a location where the double layer potential will decay to 1/*e* of its original value. Physically, this 1/*e* distance is the point where the potential energy approximately equals the thermal energy of the shielding ions [8]. This distance is called the Debye length, and is frequently used to characterize the size of the double layer.

1.3 Electrophoresis

For electrophoresis, the transport method used in this work, the physics are very similar to that of electroosmosis. When charged particles are placed into a buffer, they begin to attract charged ions from the buffer to form a double layer as in figure 2.

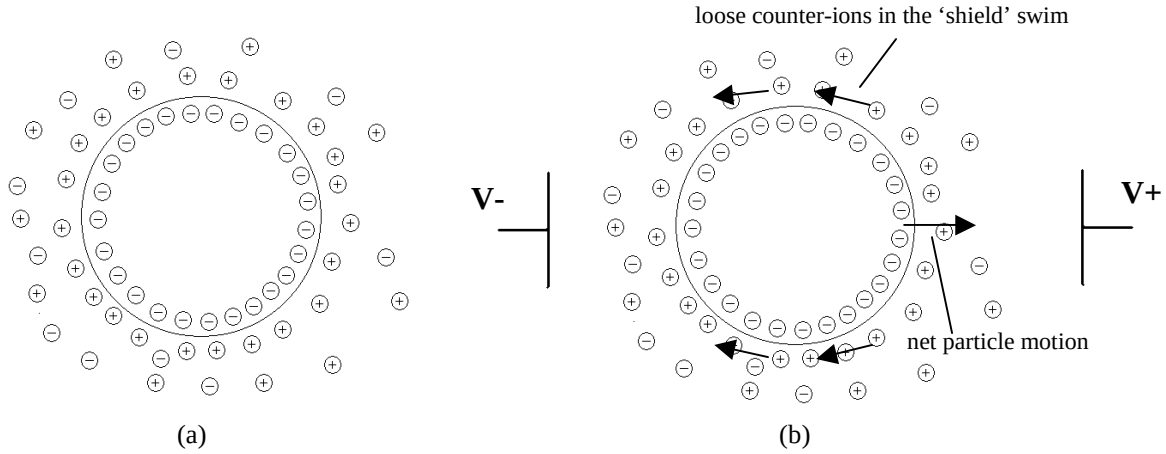

Figure 2 – (a) Double layer around charged particles in electrophoretic separation. (b) Motion of double layer and resulting net particle motion.

When an electric potential is applied to the channel, the double layer around these charged particles feels an electric force. Since the normal component of the electric field within the double layer is generally much stronger than that of the applied electric field, only the tangential component of the applied electric field has an effect on the particle [9]. This causes the mobile charge in the double layer to "swim", which exerts a viscous force on the buffer, and this propels the charged particle. For example, in figure 2, a negative(positive) potential on the left and a positive(negative) potential on the right would cause the shielding positive charge in the double layer to migrate to the left(right), which would create the viscous forces with the buffer to cause the charged particle to "swim" to the right(left). From this point of

view, it becomes apparent that electrophoretic and electroosmotic flows are complements of each other, and their analysis is mostly interchangeable [8].

1.4 Equations for the Electrophoretic Dynamics of Separation Systems

When looking at electrophoretic motion of more than just a single particle and assuming that the double layers have a small Debye length and remain undistorted in the flow, and that the flow is inertia free, the equations describing the dynamics of the species flow reduce to three. First, the electric field in the channel is described by Laplace's equation:

$$\nabla^2 \Phi = 0, \tag{2}$$

since for a small Debye length, the distance away from the charged particle before it appears completely shielded and charge neutral is not far. So for any Debye length much less than the particle radius, the particle appears uncharged at any length scale characteristic of the channel size. Second, the inertia-free motion of the species is related to the electric field through its mobility, which is described by the Helmholtz-Schmolochowski equation:

$$\vec{u} = \frac{\varepsilon \zeta \vec{E}}{\mu_v} = \mu \vec{E}, \tag{3}$$

where ε is the permittivity of the buffer, ζ is the zeta potential of the particles, μ_v is the viscosity of the buffer, and E is the electric field. Note that the combination of ε, ζ, and μ_v in (3) describes the mobility of the particles. Finally, with the inertia-free effects of diffusion, the field-coupled motion of the species concentration is described by the advection-diffusion equation:

$$\frac{\partial c}{\partial t} + \vec{u} \cdot \vec{\nabla} c = D \nabla^2 c \tag{4}$$

The remainder of this thesis will use the previous three equations, (2), (3), and (4), to analyze and produce models for serpentine separation channels. In the next chapter of this report, the field structure will be derived from (2) and analyzed for use in (3). Then, chapter 3 will explore the effects of the velocity field from (3) on the variance of the concentration distributions of analyte bands described by

(4). All of the models introduced in the following chapters of this thesis are verified within their chapter of origin. Finally, chapter 4 will provide a conclusion for this work.

Within the scope of serpentine channel electrokinetic separation systems, there are several types of designs possible. The use of modified turn geometries is proposed in [2,3], however, this thesis will focus on uniform 180^{o} turn geometries since they are still very common.

2. Electric Field Structure in Uniform Curved Microchannels

This chapter will introduce models of the electric field for serpentine channels, which gradually relax the assumptions made in [2,3,4,5]. These models will be verified with finite element software where necessary as they are developed. The next chapter will use these new models to create more accurate models of the band variance in the separation channels.

Previous work [2,3,4,5] makes two assumptions about the electric field in their single turn dispersion models. The first assumption is that the electric field's magnitude changes linearly in the radial direction within the turn, which is an approximation of a field whose magnitude varies as $1/r$ and is circumferentially directed. The second assumption is that the field changes abruptly from a constant value in the straight section to the linear circumferentially directed field in the turn. These two assumptions result in a simple linear skew of the band after the turn, whose variance is:

$$\sigma^2 = \frac{skew^2}{12}, \tag{5}$$

where $skew = 2\theta w$, which represents the length shown in figure 3, the turn angle, θ, equals π for 180^o turns, and w is the width of the channel, [11]. An interpretive comparison of the resulting band shape with and without the two assumptions made in [2,3,4,5] is shown in figure 3.

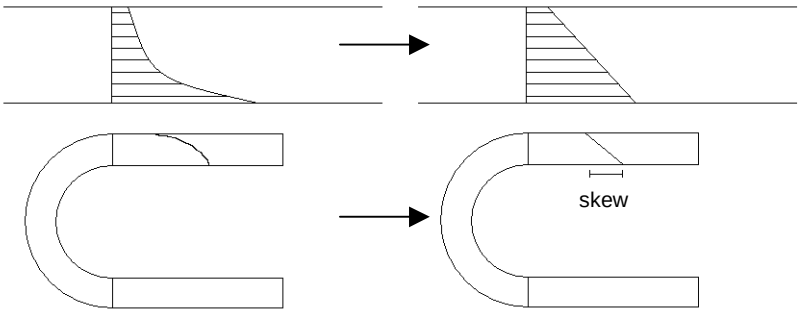

Figure 3 – Actual $1/r$ velocity profile shown on the left, linear approximation shown on the right. As the width of the channel increases, the accuracy of the linear approximation decreases.

The assumptions of a linear circumferentially directed electric field (and the resulting velocity profile) with the abrupt transition in the electric field between the straight leg and curved turns make the

analysis of microchannel dispersion much easier. However, such analysis is only valid for channels with a center radius, r_c, much greater than the width of the channel. A picture of the electric field components in a channel with a w/r_c of 1.0, along axial lines at $w/4$, $w/2$, and $3w/4$, is seen in figure 4.

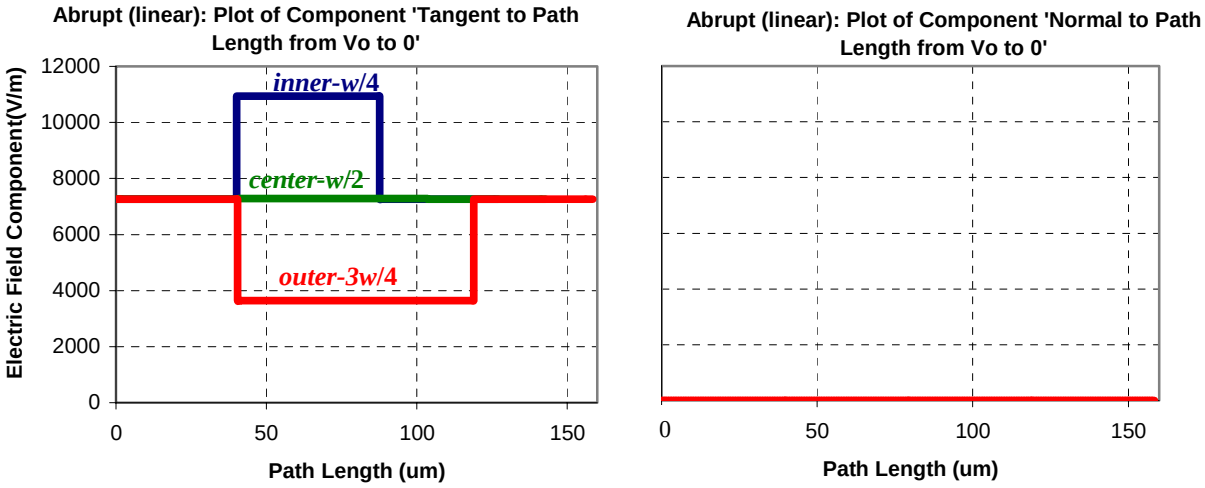

Figure 4 – Plot of the axial and transverse components of the abrupt-transition linear electric field. Note, there are no transverse components as shown in the figure on the right for the abrupt description. This is for a channel with a width-to-center radius ratio, w/r_c, of 1.0.

2.1 Abrupt-Transition 1/*r* (1-Assumption) Field Model

This section will reduce the number of assumptions made in [2,3,4,5] by not linearizing the electric field in the curve. Since the abrupt-transition assumption is still made, it is apparent that this description will also be missing information about the true structure of the electric field, as seen in the equipotential lines of figure 5a and 5b. However, since the abrupt-transition 1/*r* field structure contains more information than the simple linear models and is much easier to manipulate than a full Laplacian solution, its derivation is provided in this section. Note, that further on in this report the abrupt-transition 1/*r* field structure is commonly referred to only as an 'abrupt' or 'abrupt-transition' field structure, since the abrupt transition is its only assumption. This is different from the abrupt-transition *linearized* field structure.

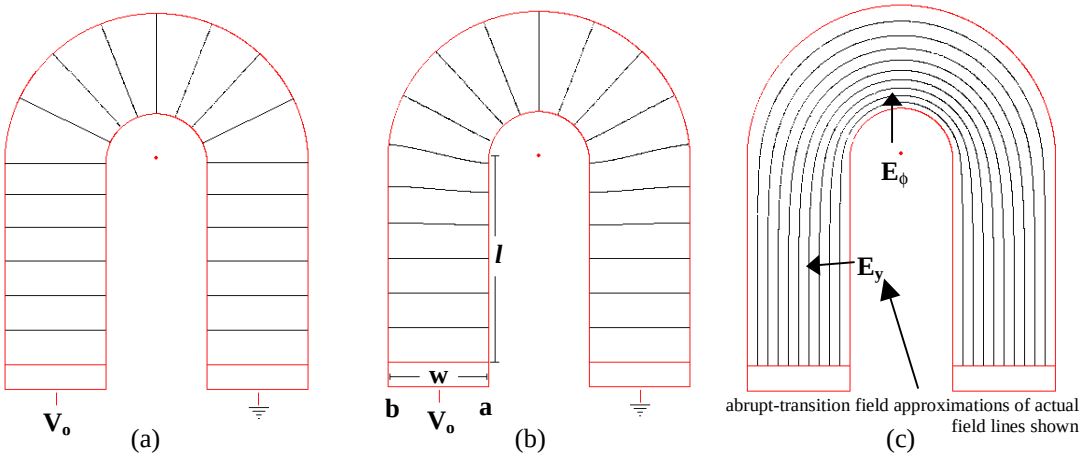

Figure 5 - (a) Abrupt-transition 1/*r* field equipotential lines (b) Laplacian electrostatic transition field equipotential lines. (c) Electric field lines corresponding to (b)

By taking the line integral of the electric field along the channel axis, setting it equal to the voltage applied between the two leg ends, and requiring the conservation of current between the straight and curved sections, the following field structure is derived:

$$E_y = \frac{V_o \ln(b/a)}{2l\ln(b/a) + w\pi} \tag{6a}$$

$$E_\phi = \frac{wV_o}{r(2l\ln(b/a) + w\pi)}, \tag{6b}$$

where *w*, *r*, *l*, *b*, *a*, and V_o are the dimensions and applied voltage as seen in figure 5b. These results show a constant field magnitude in the axial direction within the straight legs, as seen in (6a), and a 1/*r* magnitude field in the axial direction in the curved sections, as seen in (6b).

Figure 6 visualizes the abrupt-transition 1/*r* field components as described by (6a) and (6b) along axial lines at *w*/4, *w*/2 and 3*w*/4. Note first that this abrupt description has no transverse components, which completely ignores the bending of the equipotential lines around the intersection of the straight and curved sections seen in figure 5b. Second, note the nonphysical transition from the constant magnitude field in the straight legs to the 1/*r* circumferential field in the curved section. These missing components affect the variance of an analyte band traveling under the influence of the electric field through a channel,

as seen in the next chapter, and will be accounted for in the next section with a full Laplacian description of the electric field structure.

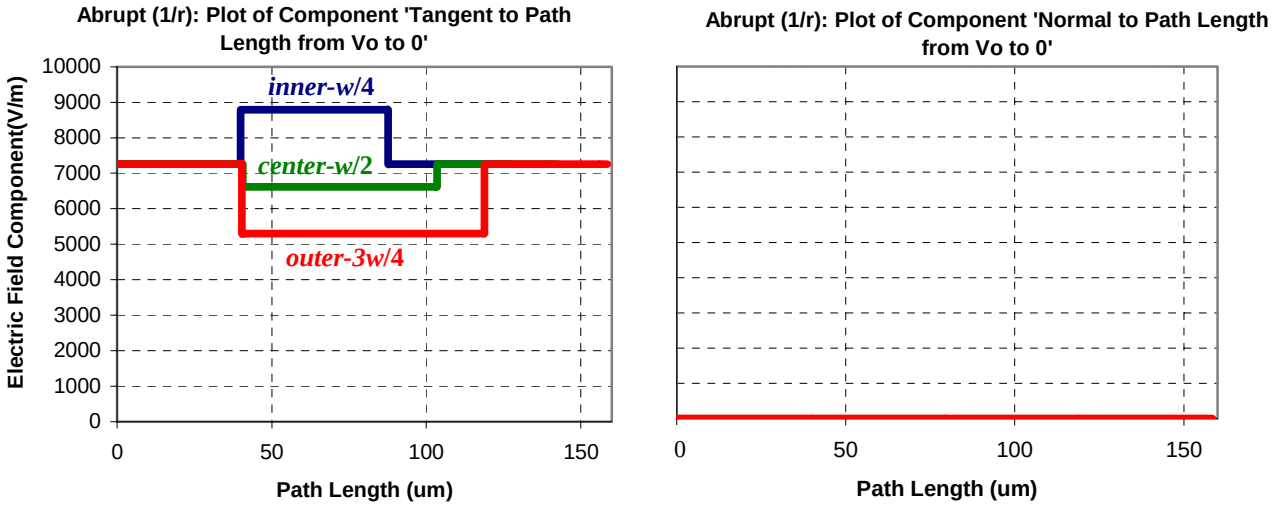

Figure 6 – Plot of the axial and transverse components of abrupt-transition 1/*r* electric field. Note, there are no transverse components as shown in the figure on the right for the abrupt-transition 1/*r* description either. This is for a channel with a width to center radius ratio of 1.0.

2.2 Continuous-Transition Laplacian (0-Assumption) Field Model

The full Laplacian solution, as seen in the equipotential lines of figure 5b, has more structure than the abrupt-transition 1/*r* solution due to the curvature of the equipotential lines before and after the straight section's intersection with the curve. Additional solutions from Laplace's equation superposed with the abrupt-transition solutions from the previous section, which are valid solutions to Laplace's equation, provide this additional structure, and a complete model that agrees well with full numeric PDE solutions of the field structure.

To derive the additional solutions to Laplace's equation, symmetry is utilized and only half of the channel is analyzed, as seen in figure 7. The analysis on this half of the channel requires splicing of the solutions in the straight and curved sections, which can be achieved with suitable boundary conditions. To obtain the correction fields, only the solutions to Laplace's equation that decay away from the intersection line will be sought, since the transition that is apparent in the equipotential lines of figure 5b

fades away leaving the abrupt-transition solutions in the curve and straight sections far from the intersection line, whose solutions we already have in (6a) and (6b).

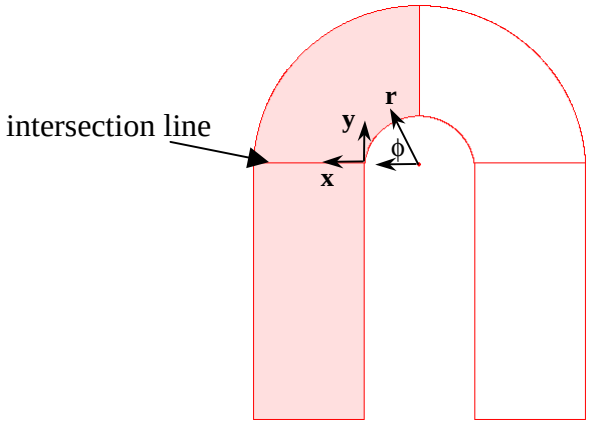

Figure 7 – The shaded region shows the only half of the channel that needs to be analyzed due to symmetry. The two different sets of axes represent the coordinate systems for the curved section and the straight section, whose solutions need to be spliced together at the intersection.

For the curved section in figure 7, Laplace's equation takes the following form:

$$\nabla^2 \Phi = 0 \tag{7a}$$

$$\frac{1}{r}\frac{\partial}{\partial r}\left(r\frac{\partial \Phi}{\partial r}\right)+\frac{1}{r^2}\frac{\partial^2 \Phi}{\partial \phi^2}=0 \tag{7b}$$

Assuming that $\Phi(r,\phi)$ is separable into independent functions of r and ϕ, and choosing the solution for the potential that has decaying exponentials in the ϕ direction, produces a potential in the curved section of the following form:

$$\Phi(r,\phi)=[A_1 e^{k\phi}+A_2 e^{-k\phi}][A_3\cos(k\ln r)+A_4\sin(k\ln r)] \tag{8}$$

Using the fact that the electric field is the negative gradient of the potential while keeping only decaying exponentials, and using the boundary conditions

$$E_r|_{r=a}=0 \text{ and } E_r|_{r=b}=0 \tag{9}$$

reduces the number of individual coefficients to be solved and results in the following series solutions for the electric field components:

$$E_r(r,\phi) = -\frac{\partial \Phi}{\partial r} = \sum_n \frac{C_n}{r} e^{-\left(\frac{n\pi\phi}{\ln(b/a)}\right)} \sin\left(n\pi \frac{\ln(r/a)}{\ln(b/a)}\right) \tag{10a}$$

$$E_\phi(r,\phi) = -\frac{\partial \Phi}{\partial \phi} = \sum_n \frac{C_n}{r} e^{-\left(\frac{n\pi\phi}{\ln(b/a)}\right)} \cos\left(n\pi \frac{\ln(r/a)}{\ln(b/a)}\right) \tag{10b}$$

The series solutions in (10) result from the boundary conditions and the periodic nature of the solution basis functions, each period of which is a partial solution and therefore added into the total series solution. Furthermore, the remaining coefficients, C_n, will be solved when the curved and straight section solutions are spliced together.

For the straight section seen in figure 7, Laplace's equation takes the following form:

$$\nabla^2 \Phi = 0 \tag{11a}$$

$$\frac{\partial^2 \Phi}{\partial x^2} + \frac{\partial^2 \Phi}{\partial y^2} = 0 \tag{11b}$$

Again, choosing the solutions that decay from the intersection line leaves us with the potential in the straight section:

$$\Phi(x,y) = B_1 \sin(kx) e^{ky} + B_2 \cos(kx) e^{ky}, \tag{12}$$

where y is always negative as defined by the x-y coordinate system in figure 7, so the exponents in (12) are decaying away from the intersection line.

Taking the negative gradient of (12) and using that to create a Fourier series approximation for the correction fields provides the x and y components of the electric field as follows:

$$E_x(x,y) = -\frac{\partial \Phi}{\partial x} = \sum_n D_n \frac{n\pi}{w} \sin\left(\frac{n\pi x}{w}\right) e^{\frac{n\pi y}{w}} \tag{13a}$$

$$E_y(x,y) = -\frac{\partial \Phi}{\partial y} = \sum_n -D_n \frac{n\pi}{w} \cos\left(\frac{n\pi x}{w}\right) e^{\frac{n\pi y}{w}}, \tag{13b}$$

where the boundary conditions

$$E_x|_{x=0} = 0 \text{ and } E_x|_{x=w} = 0 \tag{14}$$

result in the series solutions and reduce the number of coefficients, leaving only D_n, which can be solved, along with C_n in (10), when E_x, E_y, E_r, and E_ϕ are spliced at the intersection line. When the correction factor components in (10) and (13) are superposed with the abrupt-transition 1/r field solutions from (6) to provide the correct field structure far from the intersection line, the result is the following set of equations:

$$
\begin{aligned}
E_r^{curve} &= \sum_n \frac{C_n}{r} \exp\left(\frac{-n\pi\phi}{\ln(b/a)}\right) \sin\left(n\pi \frac{\ln(r/a)}{\ln(b/a)}\right) \\
E_\phi^{curve} &= \frac{wV_o}{r(2l\ln(b/a)+w\pi)} + \sum_n \frac{C_n}{r} \exp\left(\frac{-n\pi\phi}{\ln(b/a)}\right) \cos\left(n\pi \frac{\ln(r/a)}{\ln(b/a)}\right) \\
E_x^{straight} &= \sum_n D_n \frac{n\pi}{w} \sin\left(\frac{n\pi x}{w}\right) \exp\left(\frac{n\pi y}{w}\right) \\
E_y^{straight} &= \frac{V_o \ln(b/a)}{2l\ln(b/a)+w\pi} - \sum_n D_n \frac{n\pi}{w} \cos\left(\frac{n\pi x}{w}\right) \exp\left(\frac{n\pi y}{w}\right)
\end{aligned}
\tag{15}
$$

The components in (15) represent the field in both the straight and curved sections, and are effectively coupled at the intersection line by solving for the remaining coefficients, C_n and D_n, using the boundary conditions $E_\phi|_{\phi=0}=E_y|_{y=0}$ and $E_r|_{\phi=0}=E_x|_{y=0}$. The number of coefficients to be solved will depend on the number of terms kept in each of the series in (15). Keeping the first term in the Fourier series for both the axial and transverse components in the straight and curved sections (represented as 1x1, where the first number is the number of terms kept for the curved channel's field components and the second number is the number of terms kept for the straight channel's field components) provides sufficient accuracy for most designs, as seen in Figures 8 and 9.

To find the coefficients for an arbitrary number of Fourier components in each section, the system of equations defining the coefficients in (15) is combined in a relational form dependent on the appropriate intersection line boundary conditions into a coupling block matrix. This creates the following linear system, used to solve for C_n and D_n:

$$\begin{bmatrix} C_1 \\ C_2 \\ \vdots \\ C_n \\ D_1 \\ D_2 \\ \vdots \\ D_m \end{bmatrix} = \begin{bmatrix} \xi_{11} & \xi_{12} & \cdots & \xi_{1n} & k_1 & 0 & \cdots & 0 \\ \xi_{21} & \ddots & & \vdots & 0 & k_2 & \ddots & \vdots \\ \vdots & & \ddots & \vdots & \vdots & \ddots & \ddots & 0 \\ \xi_{m1} & \cdots & \cdots & \xi_{mn} & 0 & \cdots & 0 & k_m \\ \eta_{11} & \eta_{12} & \cdots & \eta_{1n} & -k_1 & 0 & \cdots & 0 \\ \eta_{21} & \ddots & & \vdots & 0 & -k_2 & \ddots & \vdots \\ \vdots & & \ddots & \vdots & \vdots & \ddots & \ddots & 0 \\ \eta_{m1} & \cdots & \cdots & \eta_{mn} & 0 & \cdots & 0 & -k_m \end{bmatrix}^{-1} \begin{bmatrix} \tau_1 \\ \tau_2 \\ \vdots \\ \tau_m \\ 0 \\ \vdots \\ \vdots \\ 0 \end{bmatrix}, \tag{16}$$

where k_i are simply spatial frequency relations, $i\pi/w$, m is the number of terms kept in the series for the straight section, n is the number of terms kept in the series for the curved section, and the coefficients ξ, η, and τ are solved for in the fairly standard method of determining the coefficients of Fourier series. The orthogonality of the trigonometric basis functions allows a particular coefficient to be isolated by multiplying the entire series by the desired basis function with the desired frequency and integrating over the respective period. When the series is integrated over the period, it provides the solution for the desired coefficients, ξ, η, and τ, which are related to each other by the linear system in (16). The generalized results for the coupling matrix coefficients are:

$$\begin{aligned} \xi_{ij} &= \frac{2}{w}\int_0^w \frac{1}{x+a}\cos\left(j\pi\frac{\ln(x/a+1)}{\ln(b/a)}\right)\cos\left(\frac{i\pi x}{w}\right)dx \\ \eta_{ij} &= \frac{2}{w}\int_0^w \frac{1}{x+a}\sin\left(j\pi\frac{\ln(x/a+1)}{\ln(b/a)}\right)\sin\left(\frac{i\pi x}{w}\right)dx \\ \tau_i &= \frac{2}{w}\int_0^w \left(\frac{V_{app}\ln(b/a)}{2l\ln(b/a)+w\pi}\right)\left(1-\frac{w}{(x+a)\ln(b/a)}\right)\cos\left(\frac{i\pi x}{w}\right)dx \end{aligned} \tag{17}$$

Each of the four square sub-blocks in the coupling matrix of (16) has dimensions which depend on the number of Fourier terms kept in each of the curved or straight sections. The two left sub-blocks are mxn matrices, the two right sub-blocks are mxm, and the solution vector consists of m+n elements.

As a simple example, when the number of Fourier components is equal to 1x1, the following results for C_1 and D_1 are obtained:

$$\begin{bmatrix} C_1 \\ D_1 \end{bmatrix} = \begin{bmatrix} \frac{2}{w}\int_0^w \frac{1}{x+a}\cos\left(\pi\frac{\ln(x/a+1)}{\ln(b/a)}\right)\cos\left(\frac{\pi x}{w}\right)dx & \frac{\pi}{w} \\ \frac{2}{w}\int_0^w \frac{1}{x+a}\sin\left(\pi\frac{\ln(x/a+1)}{\ln(b/a)}\right)\sin\left(\frac{\pi x}{w}\right)dx & -\frac{\pi}{w} \end{bmatrix}^{-1} \begin{bmatrix} \frac{2}{w}\int_0^w (Eso)\left(\frac{w}{(x+a)\ln(b/a)}-1\right)\cos\left(\frac{\pi x}{w}\right)dx \\ 0 \end{bmatrix} \quad (18)$$

Figure 8(a) shows the magnitude of the axial electric field components for a geometry whose width-to-center radius ratio, w/r_c, is 1.0, which is at one extreme end of the feasible design space, keeping one Fourier term for the electric fields in the curved and straight sections, (1x1). Figure 8(b) shows the results of keeping three Fourier terms for the electric field components in the curved and straight sections, (3x3). Figure 9 shows that for a width-to-center radius ratio of 0.4, which is a more reasonable upper limit to the design space [4], keeping only one Fourier component achieves excellent agreement with numeric PDE solutions for the field structure.

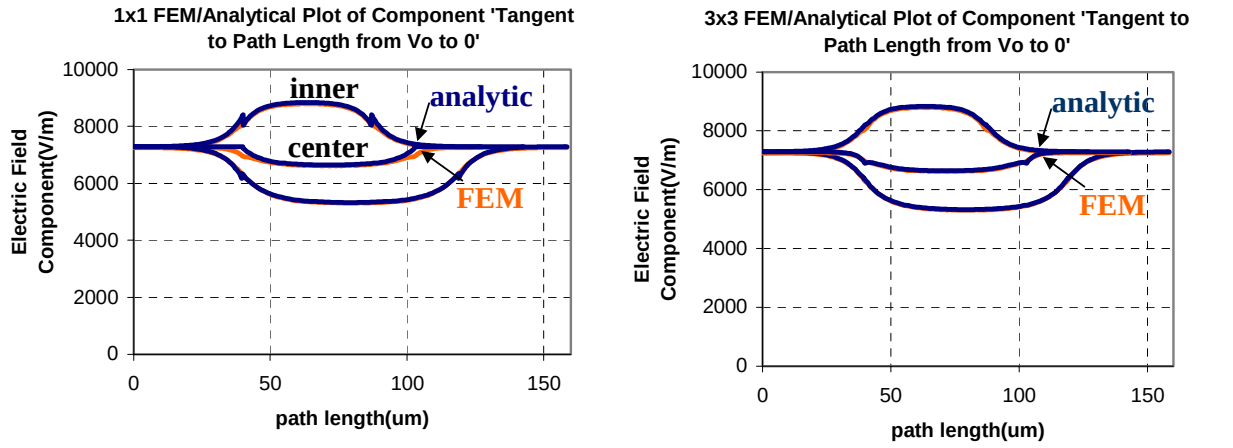

(a) (b)

Figure 8 – For a width-to-center radius ratio (w/r_c) of 1.0, figure 8(a) shows the axial component of the electric field using one Fourier term for curved section field components and the straight section field components (1x1). figure 8(b) shows the same comparison using three Fourier terms for the curved and straight section field components (3x3).

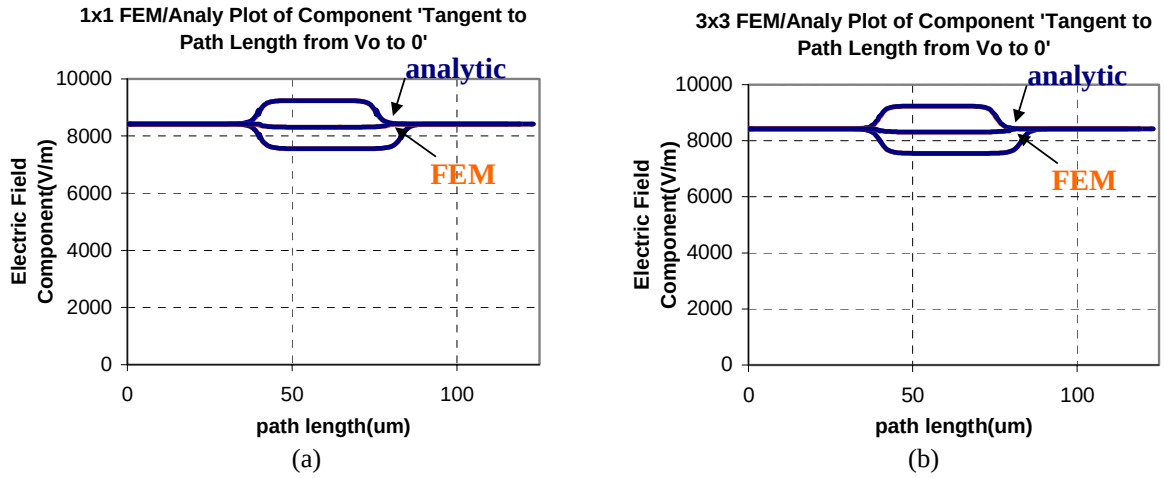

Figure 9 – For a width-to-center radius ratio (w/r_c) of 0.4, figure 9(a) shows the axial field component result for 1x1 Fourier terms, and figure 9(b) shows the results for 3x3 Fourier terms. For smaller w/r_c ratios the accuracy of the analytic field expressions in (15) increases for a given number of Fourier terms.

One final observation that can be made from the Laplacian derivation is the persistence of the transition field components away from the intersection line of the channel sections. This persistence is important for measuring the turn-induced variance because the band must be outside of the transition fields before the turn-induced variance is complete and a measurement can be made. Looking at (15), it can be seen that the transition components have exponential decay factors, which can be used to determine how far the transition fields persist from the intersection line. The transition fields fall to 4% of their original value at about a channel's width length into the straight section, and they fall to about 4% of their original value at about a channel's width arc-length into the curved section along the center radius. This decay rate is for the first harmonic of the Fourier series, which is the least attenuated of all the harmonics. So after a channel's width length in both directions from the intersection line along the center radius (shown in figure 10), the transition fields have decayed so that the field structure is essentially defined by the abrupt-transition $1/r$ field description.

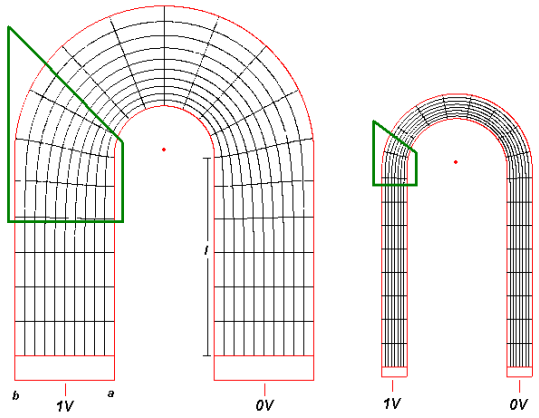

Figure 10 – The persistence of the transition fields from the intersection line, highlighted in the green boxes, for geometry with a width-to-center radius, w/r_c ratio of 1.0 on the left and a w/r_c of 0.4 on the right.

To make the final comparison with the abrupt-transition field results seen in figure 6, figure 11 shows the axial and transverse components of the Laplacian field structure, for w/r_c=1.0 along axial lines at $w/4$, $w/2$, and $3w/4$, which now accounts for the missing field structure.

In summary, this chapter has shown two models of the electric field structure for serpentine channels gradually reducing the assumptions found in [2,3,4,5]. The effect the new field structure has on the variance of a band will be shown in the next chapter.

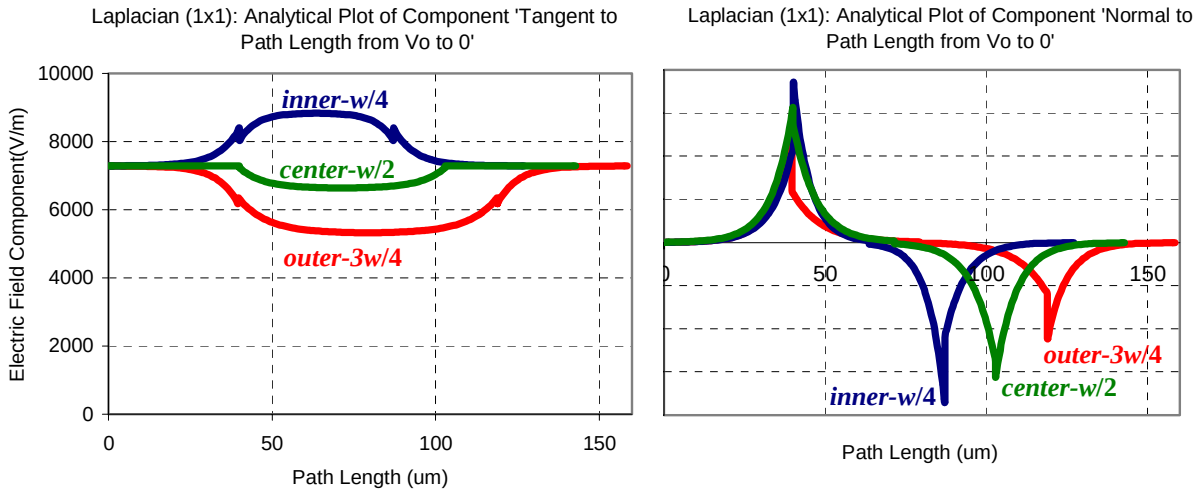

Figure 11 – A plot of the axial (on the left) and transverse (on the right) components of the electric field as described by the Laplacian derivation in Eq. 8. Compared to Figure 2, there is a smoother transition between the straight and curved section field structure on the left, and the transverse components on the right, missing in Figure 2, are now present.

3. Analyte Dispersion Results

This chapter will use the electric field models developed in the previous chapter to create models of the variance of the analyte band as it travels through the serpentine separation channel, which is a common separation topology [3]. The serpentine channels are simply complementary connections of the single turns and straight sections seen in the previous chapter, as shown in figure 12. The method of measuring the variance of the band will be laid out, followed by a description of the various operating regimes of the separation system. A variance model using the abrupt-transition $1/r$ fields developed in the previous chapter will then be created and used to generate a model using the continuous-transition Laplacian fields, also developed in the previous chapter. Comparisons to FEMLAB numerical PDE simulations are made as they are needed. Finally, there are several sources of dispersion in serpentine separation systems, such as the injector, detector, electric field structure, geometry and diffusion. The models in this chapter focus on the electric field structure and geometry as sources of dispersion, since such sources arise from serpentine topologies.

3.1 Measuring Dispersion

The process of measuring the dispersion of a continuous concentration distribution is essential to creating models of separation systems. This section introduces the measurement method used for the models in this report.

Real systems measure the dispersion of an analyte band in a channel with various sensors ranging from 2-dimensional (2-D) CCD arrays to laser scanning single-point optical devices [12]. These sensor devices have practical experimental limitations such as the resolution of the pixels in the CCD and the wavelength of the laser-scanning element. These limitations are usually characterized and modeled as an additional source of dispersion in the system. Since injectors and detectors are not the focus of this work, only the effects of the serpentine channels are included in the calculation and derivation of models of the band dispersion. Injection and detector variance models will be the focus of later work.

For a continuous 2-D concentration distribution, the method of determining the analyte variance is summarized in figure 12. The concentration distribution is reduced to a *y*-dependent 1-dimensional (1-D) concentration profile by averaging along the x-axis. Then the variance of this 1-D profile is found using the standard formula shown in figure 12.

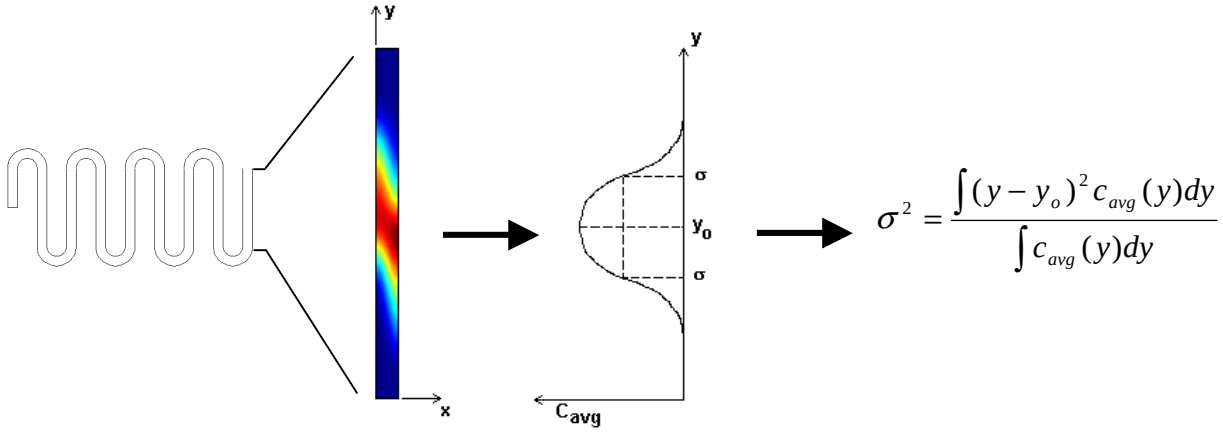

Figure 12 – The process of converting a concentration distribution into a measure of variance.

3.2 Non-Dimensional Serpentine Channel Parameters

This section will first show a non-dimensionalization of the advection-diffusion equation, which describes the dynamics of the separation channels. Then a complete set of non-dimensional characteristic parameters will be derived using the Buckingham π-Theorem. These steps are useful for gaining an intuitive understanding of how the separation systems operate.

The dynamics of the analyte band traveling through a channel are described by the advection-diffusion partial differential equation, repeated from (4) here:

$$\frac{\partial c}{\partial t} + \vec{u} \cdot \vec{\nabla} c = D \nabla^2 c \qquad (19a)$$

Non-dimensionalizing (19a) gives

$$\frac{\partial c^*}{\partial t^*} + \vec{u}^* \cdot \vec{\nabla}^* c^* = \frac{1}{Pe} \nabla^{*2} c^*, \qquad (19b)$$

where

$$c^* = \frac{c}{c_o} \quad u^* = \frac{\vec{u}}{u_o} \quad x^* = \frac{x}{w} \quad y^* = \frac{y}{w} \quad t^* = \frac{t}{w/u_o} \tag{20}$$

In the non-dimensional form of (19b), the balance between the advection and diffusion terms more evidently describes the dynamics of a system. In this case, the Peclet number describes this balance between advection and diffusion, where

$$Pe = \frac{u_o w}{D}, \tag{21}$$

and the concentration, length, and time dimensions have been scaled by characteristic parameters, shown in (20), such as the initial concentration, c_o, the width of the channel, w, and the ratio of the channel width to mean velocity, w/u_o, respectively. Here the mean velocity, u_o, is the mobility times the abrupt-transition $1/r$ field value in the straight sections, E_y, which is the mean field strength for the entire channel, including the curves. This type of dimensional analysis in (19) can be used to identify four basic regimes in which the system can operate, depending on its characteristic non-dimensionalized parameters. In this case, the Peclet number is one of the characteristic non-dimensional parameters.

To discover any additional non-dimensional parameters that characterize the operating regime, the Buckingham π-Theorem can be utilized, as shown in the Appendix. Based on the physical parameters describing the band variance of a serpentine microfluidic system, such as the channel width (w), turn center radius (r_c), length between complementary turns (L_{bt}), the electric field strength (E_o), diffusivity (D), and species mobility (μ), the following maximal set of three non-dimensional terms fully characterize the system: r_c/w, L_{bt}/w, and $u_o w/D$. Where $u_o w$/D is recognized as the Peclet number based on channel width. Defining the non-dimensional parameters $T_{bt}=wPe/L_{bt}$ (the ratio of the time it takes a particle to travel the width of the channel to the time it takes a particle to travel the length between turns) and $T_t=wPe/(\pi r_c)$ (the ratio of the time it takes a particle to travel the width of the channel to the time it takes a particle to travel the length of the turn along r_c), three equivalent non-dimensional parameters are: T_{bt}, T_t, and w/r_c. These parameters can be used to fully characterize the regimes in the problem space of the separation system, as seen in the next section.

3.3 System Dispersion Regimes

This section will introduce the various regimes in which the separation system can operate, followed by several examples using FEMLAB.

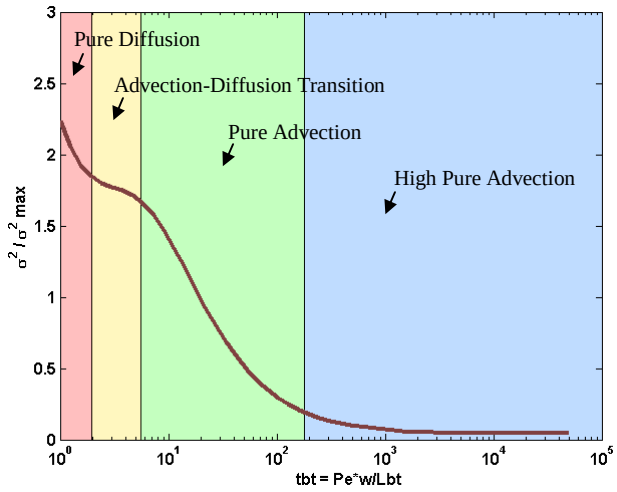

Figure 13 – FEMLAB simulations created that span the T_{bt} space crossing four identifiable regimes, which go from left to right, red to blue, as the pure diffusion, advection-diffusion transition, pure advection, and high-pure advection regimes.

The four regimes are easily identified in the graph by the three knees separating the regimes with four different characteristic slopes. The four regimes from left to right are: Pure diffusion, advection-diffusion transition, pure advection, and high-pure advection. The pure diffusion regime is characterized by the band being always homogenous orthogonal to the channel axis and widening along the channel axis. The advection-diffusion transition region is characterized by the band being mostly homogenous, but experiencing some skewing from advection around the turns. However, in this regime there is not enough advection dominance to permit unskewing after complementary turns. In the pure advection regime, the band strongly expresses skewing and advection is now dominant enough to permit some unskewing of the band, i.e., some dispersion reduction, however, axial band widening is still present. In the high-pure advection regime, the analyte bands strongly express skewing and unskewing after turns, a characteristic parabolic-like shape after complementary turns, and no significant widening of the band from diffusion. Figures 14a through 14d show examples of bands traveling in each of these regimes.

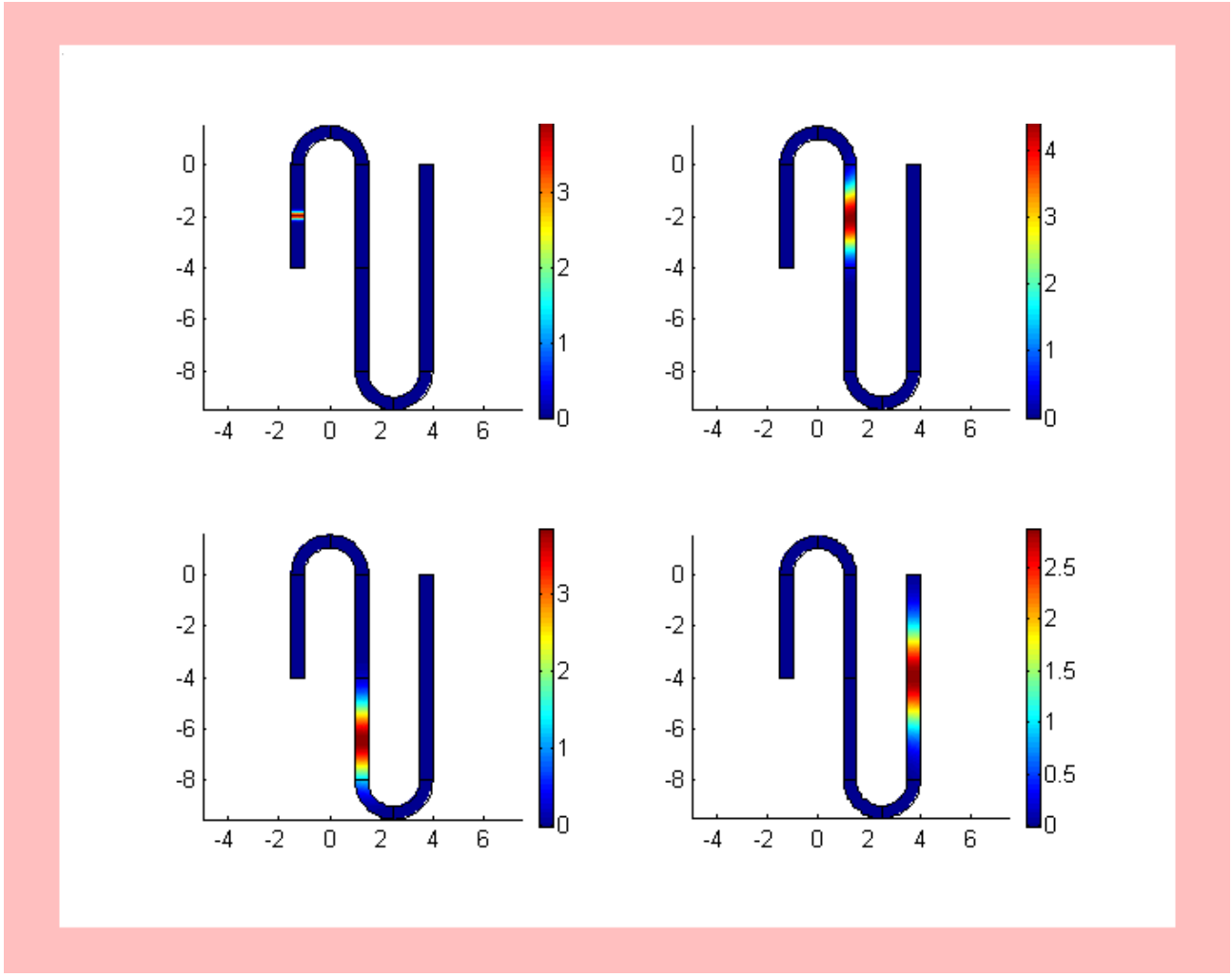

Figure 14a – Examples of the various regimes. This figure shows the pure diffusion regime in the red section of figure 13. The band shows no skewing after turns and maintains essentially a 1-D concentration gradient along the channel axis. Note the band has traveled from the middle of the first leg to the middle of the last leg.

Table 1 – System parameters for figure 14a.

b	a	w	μ	E_y	D	L_{inj}	L_{bt}	L_{det}
Outer radius	Inner radius	Channel width	Species mobility	Straight leg electric field	Diffusivity	First straight leg length	Length between turns	Last straight leg length
15 µm	10 µm	5 µm	$1.5 \cdot 10^{-7}$ m^2/Vs	8420.17 V/m	$3.9470 \cdot 10^{-10}$ m^2/s	40 µm	80 µm	80 µm

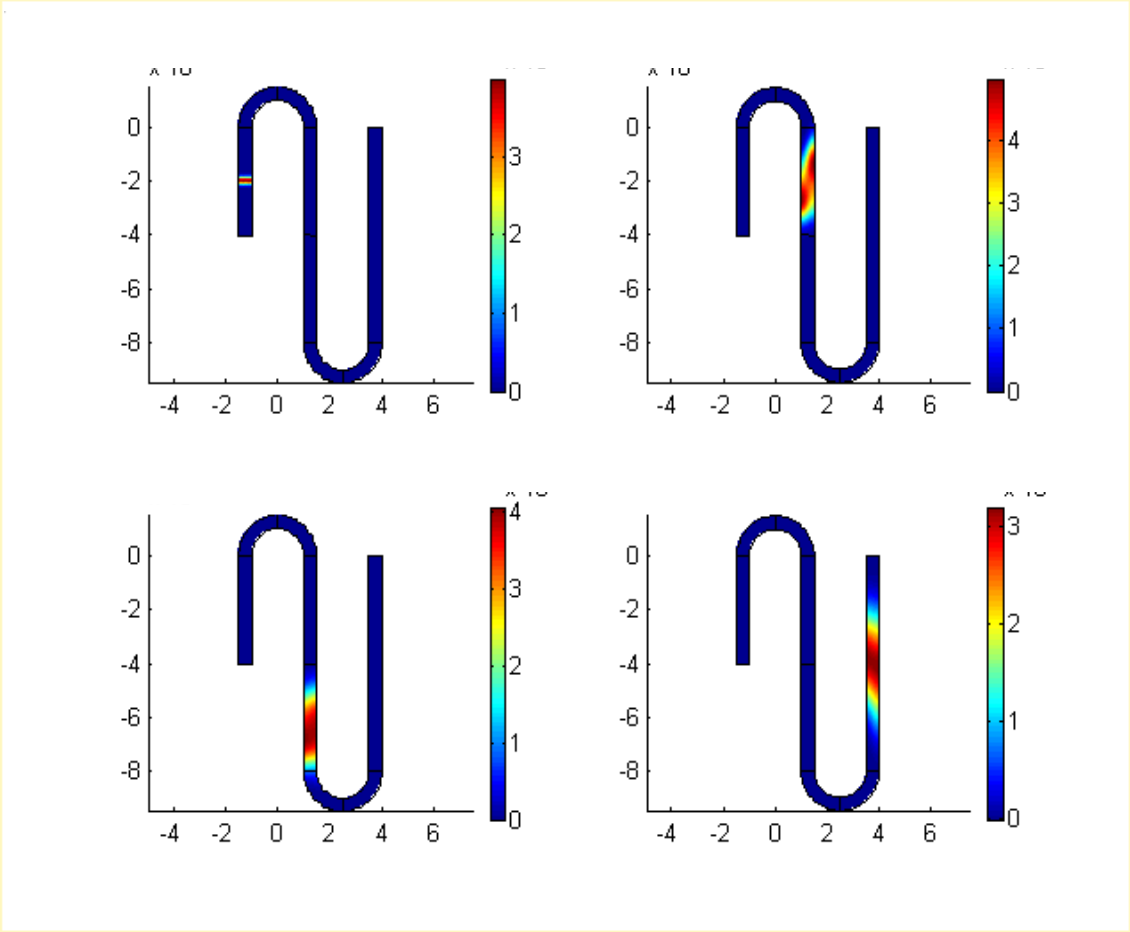

Figure 14b – Examples of the various regimes. This figure shows the advection-diffusion transition regime in the yellow section of figure 13. There is skewing after a turn, but significant transverse diffusion remains that keeps the band fairly homogeneous across the channel width and significant axial diffusion spreads the band axially. Therefore, complementary turns cannot unskew the band, but instead "overskew" the band. Note the band has traveled from the middle of the first leg to the middle of the last leg.

Table 2 - System parameters for figure 14b.

b	a	w	μ	E_y	D	L_{inj}	L_{bt}	L_{det}
Outer radius	Inner radius	Channel width	Species mobility	Straight leg electric field	Diffusivity	First straight leg length	Length between turns	Last straight leg length
15 μm	10 μm	5 μm	$1.5 \cdot 10^{-7}$ m^2/Vs	8420.17 V/m	$1.3085 \cdot 10^{-10} m^2/s$	40 μm	80 μm	80 μm

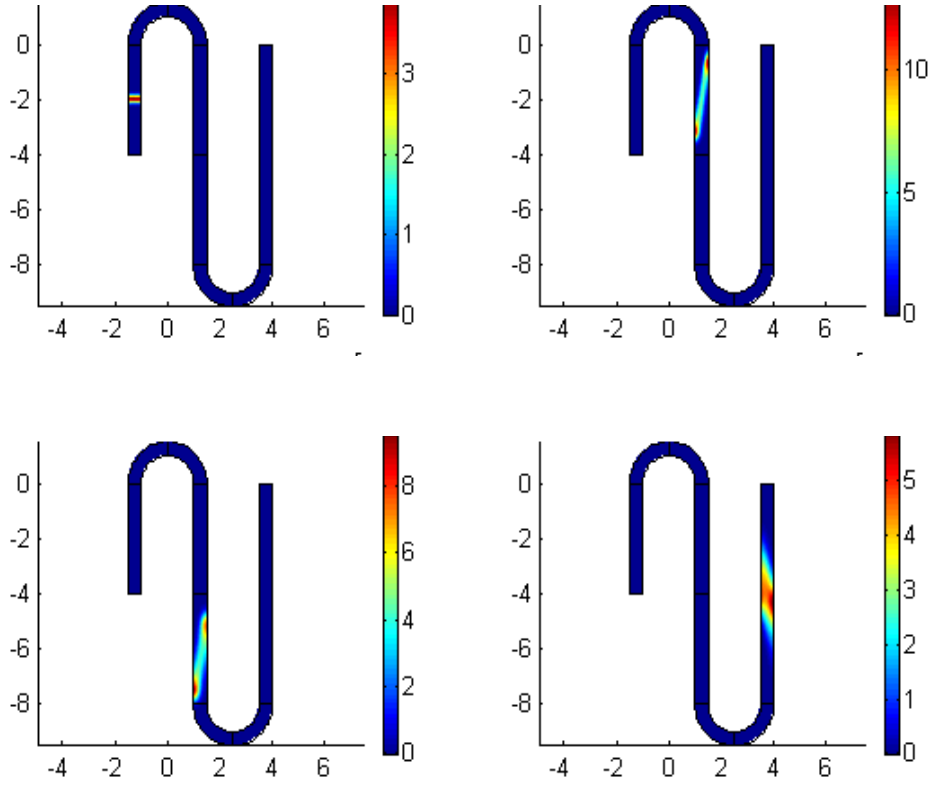

Figure 14c – Examples of the various regimes. In the pure-advection regime shown here, representing the green region of figure 13, there is significant skewing of the band after a turn and transverse diffusion is small enough to prevent the band from homogenizing across the channel width. The field effects are dominant enough over diffusion to allow some unskewing after complementary turns, some "overskewing" is still present, and axial diffusion is still present enough to spread the band axially. Note the band has traveled from the middle of the first leg to the middle of the last leg.

Table 3 - System parameters for figure 14c.

b	a	w	μ	E_y	D	L_{inj}	L_{bt}	L_{det}
Outer radius	Inner radius	Channel width	Species mobility	Straight leg electric field	Diffusivity	First straight leg length	Length between turns	Last straight leg length
15 µm	10 µm	5 µm	$1.5 \cdot 10^{-7}$ m^2/Vs	8420.17 V/m	$1.7935 \cdot 10^{-11}$ m^2/s	40 µm	80 µm	80 µm

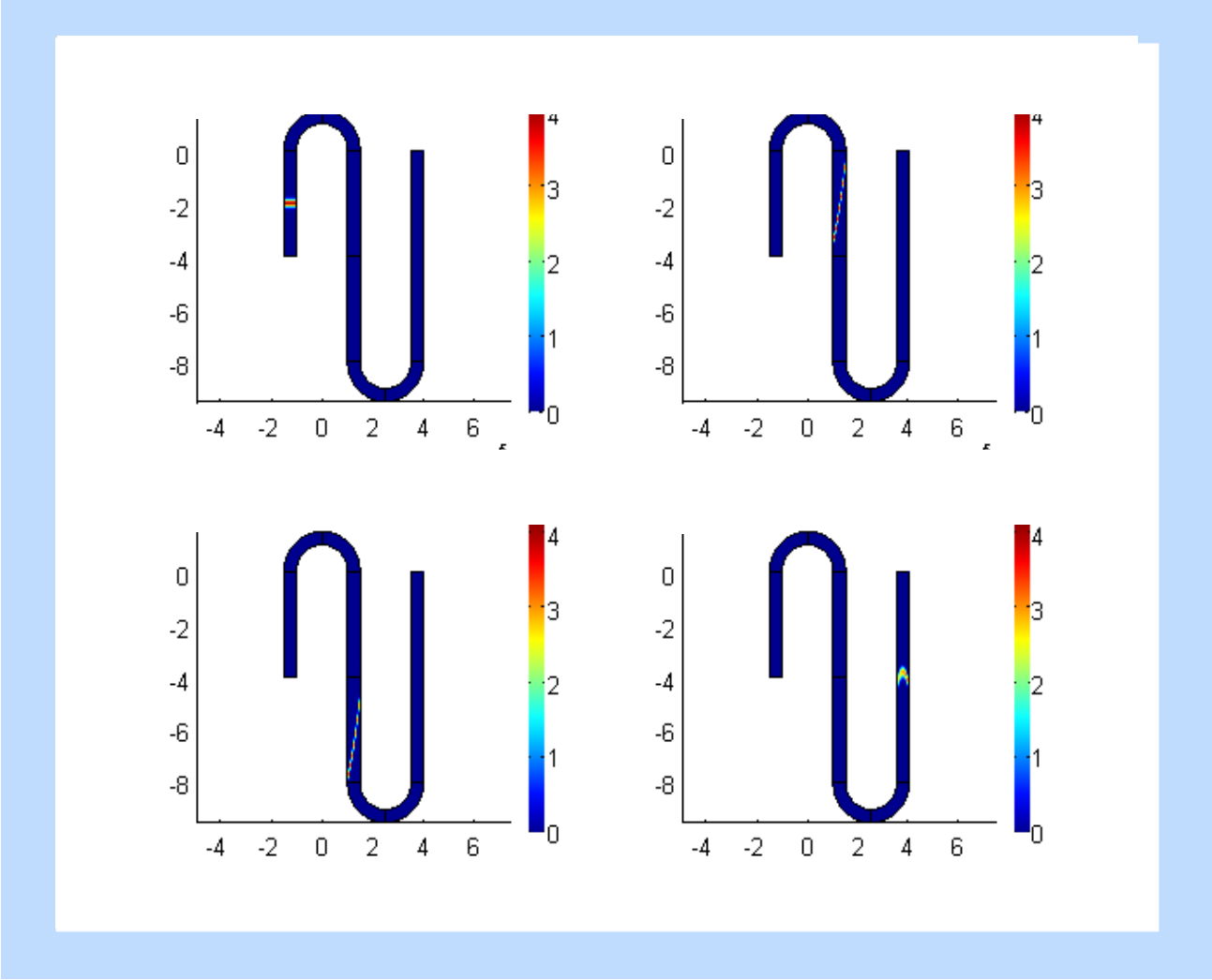

Figure 14d – Examples of the various regimes. The last regime, shown in this figure and representing the blue region in figure 13, is the high-pure advection regime. In this regime, the effects of diffusion are negligible, so there is no significant widening of the band axially or transversely. The effects of the geometry and field structure define the skew and unskew of the band. The unskewing of the band after complementary turns results in the characteristic parabolic shape. Note the band has traveled from the middle of the first leg to the middle of the last leg.

Table 4 - System parameters for figure 14d.

b	a	w	μ	E_y	D	L_{inj}	L_{bt}	L_{det}
Outer radius	Inner radius	Channel width	Species mobility	Straight leg electric field	Diffusivity	First straight leg length	Length between turns	Last straight leg length
15 µm	10 µm	5 µm	$1.5 \cdot 10^{-7}$ m^2/Vs	8420.17 V/m	$8.9570 \cdot 10^{-14}$ m^2/s	40 µm	80 µm	80 µm

Most microfluidic designs lie within the pure and high-pure advection regimes (green and blue) [3]. Out of these two regimes, the majority of systems would fall into the pure-advection regime. However, there are still some very important examples that fall into the high-pure advection regime. For example, a typical example of a system found in the high-pure advection regime is DNA electrophoresis where a sieving matrix is employed, as seen in [12]. A typical Peclet number for such systems is around 15,000. Within the scope of these regimes, the next section will present analysis starting with the abrupt-transition $1/r$ field structure to analytically determine the variance of a band as it travels through serpentine channels within the high-pure advection regime. Further sections will begin to look at the regimes with where diffusion is more important.

3.4 High-Pure Advection Analytical Dispersion with 1-Assumption Field Model

Using the concepts introduced in the previous sections of this chapter, this section will produce an analytical model of the high Peclet dispersion in serpentine channels with any number of turns and the abrupt-transition $1/r$ electric field structure. This model will then be used to explore several previously unpredicted physical phenomena.

For bands traveling though the serpentine channels in the high-pure advection regime, we can ignore the effects of diffusion. Band variance is therefore determined only by the channel geometry and field structure. To analyze the abrupt-transition field dispersion, only the curved sections need to be considered, since the uniform fields in the straight sections do not contribute to the dispersion when diffusion is ignored. To find the variance of a band traveling through a serpentine channel, the band can be thought of as individual ‘particles’ following an axial path through the channel. The differences in the travel time through the curves for ‘particles’ spread across the width of the channel will serve as a measure of the band variance after traveling through the channel.

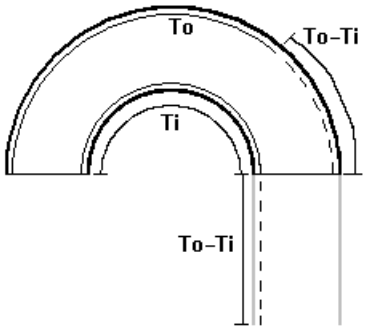

Figure 15 – The difference in times of outer and inner particles traveling through a single turn.

The time it takes a particle at radius r to travel through the channel is the distance divided by the velocity,

$$T(r) = \frac{\pi r}{\mu E_\phi(r)}, \tag{22}$$

where μ is the particle mobility and E_ϕ is the circumferential field in the curve using the abrupt-transition description in (6b), which also depends on r. So the particle along the inner most radius, a, takes $T_i = \pi a/[\mu E_\phi(a)]$ seconds and the particle along the outer most radius takes $T_o = \pi b/[\mu E_\phi(b)]$ seconds. Their difference is $T_o - T_i = [\pi/\mu][b/E_\phi(b) - a/E_\phi(a)]$, which is the time spent by the band traveling in the straight section immediately after the curve. Therefore, the time any given particle spends in the straight section after the curve is given by:

$$\Delta T(r) = \frac{\pi}{\mu}\left(\frac{b}{E_\phi(b)} - \frac{r}{E_\phi(r)}\right) \tag{23}$$

This ΔT, in (23), multiplied by the uniform velocity in the straight section gives the distance traveled by each particle in the uniform straight section:

$$\Delta L(r) = \mu E_y \Delta T(r) = \frac{\pi \ln(b/a)}{w}[b^2 - r^2], \tag{24}$$

where a, b, and w are the dimensions as defined in figure 5b.

Using (24), the variance of the profile about its mean using the sample variance,

$$\sigma_{ab}^2 = \frac{1}{w}\int_a^b (\Delta L(r) - \Delta L_{avg})^2 \, dr \,, \tag{25}$$

gives the following result for a single 180° turn with zero initial variance:

$$\sigma_{ab}^2 = \left(\frac{a^2}{3} + \frac{aw}{3} + \frac{4w^2}{45}\right)\pi^2 \ln^2\left(1 + \frac{w}{a}\right) \tag{26}$$

A similar procedure as above can be used to derive the variance for any number of turns. For this derivation, however, the absolute time spent in the curve, (22), and its effect on the displacement in the straight section after the turns is used to calculate the variance. Since the variance is a centered moment, whether or not the outer radius length or time is subtracted out has no effect on the resulting variance. This greatly simplifies the algebra, but does not give physical significance to the real displacement of the particles, since using the time spent in the curves will result in a displacement in the straight section appearing inverted. For example, for a single turn, an inner radius particle has the shortest travel time through the turn, so it will have the shortest length afterwards if this time spent in the curves is used to extend the particles into the straight section. This is obviously inverted from the physical result, since the innermost particle should be the furthest ahead in the straight section. So, a physical interpretation of the particle displacements requires that the time used to extend the particles into the straight section is the outer radius particle time minus the particle time traveling at a desired radius, as mentioned for the results in (24)-(26). For the general case of *n* turns, the physical displacements of the particles is given by:

$$\Delta L(r) = \frac{\pi \ln(b/a)}{w}\left[N_1(b^2 - r^2) + N_2\left((w + 2a - b)^2 - (w + 2a - r)^2\right)\right] \tag{27}$$

However, to find the variance using a simpler form of displacement, the time spent in the curves is utilized to find the distance traveled in the straight section, which results in the following:

$$L(r) = \frac{\pi \ln(b/a)}{w}\left[N_1 r^2 + N_2 (w + 2a - r)^2\right], \tag{28}$$

Since (28) is simply a constant minus (27), they both have the same variance. (28) is then used in the sample variance equation:

$$\sigma_{ab}^2 = \frac{1}{w}\int_a^b (L(r) - L_{avg})^2 \, dr \,, \tag{29}$$

which gives the following result for the variance with the abrupt-transition 1/*r* electric fields for *n* complementary turns:

$$\sigma_{ab}^2 = \frac{\pi^2 \ln^2(b/a)}{w^3}\int_a^b \left(N_1 r^2 + N_2 (w + 2a - r)^2 - \frac{(N_1 + N_2)((w+a)^3 - a^3)}{3w} \right)^2 dr \,, \tag{30}$$

where

$$N_1 = \frac{n + \mathrm{mod}(n,2)}{2} \,, \tag{31}$$

$$N_2 = \frac{n + \mathrm{mod}(n+1,2) - 1}{2} \,, \tag{32}$$

and *r* is the radius starting in the first curve, *n* is the number of turns, and mod(*n*,2) is the modulus after division function that gives the remainder of *n*/2. To see the complete expanded solution of (30), refer to the Appendix.

A quick example of (30) shows that for a single set of complementary turns the following fairly simple result is produced:

$$\sigma_{ab}^2 = \frac{1}{45}\pi^2 w^2 \ln^2(b/a) \tag{33}$$

Several interesting results are now apparent. First, figure 16 shows the resulting band edge after a single set of complementary turns. It shows that with the 1-assumption electric field model with the abrupt transition in the field structure between channel sections, unskewing is not complete and leaves a parabolic-like shape after complementary turns. Whereas the 2-assumption models in [2,3,4,5] with the abrupt transition in the field between channel sections and the linear electric field in the turn, predict a complete unskewing of the band after complementary turns.

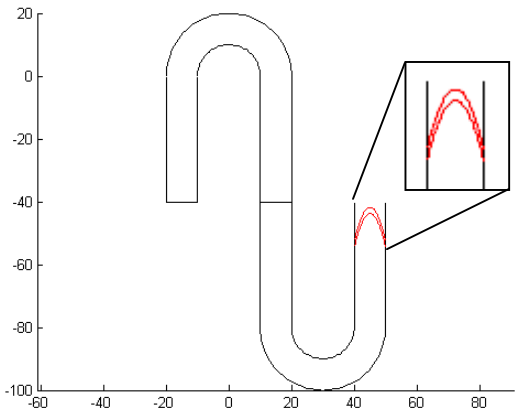

Figure 16 - Band shape after a set of complementary turns, traveling from left to right. A distorted band results, unlike when using a linear description of the field structure. A Matlab particle simulation created these results, which will be fully described in the next section.

The resultant band shape is symmetric about the center of the channel, but part of what contributes to the parabolic shape is the non-symmetry of the electric field in the turn about the central channel axis and such interaction from turn to turn. This non-symmetry occurs because the field's mean value is not precisely in the center of the channel, but at a radius less than the center. Since the complementary turns mirror the curvature of the previous turn, but the fields are different at the center of the channel, the center of the band gets and *stays* further ahead than the two band edges, which both symmetrically experience the long path-length and lessened field-strength of the outer radius of the channel. If the field were symmetric about the center of the channel, then each particle would have experienced the same electric field as its mirrored partner from the previous channel, thereby equalizing the effects from the previous turn and flattening the band. This is the case with any linear velocity profile, as opposed to any non-linear profile that is not symmetric about its mean.

Another interesting observation, shown in figure 17, is that as the number of complementary turns continues to grow, the resulting variance from the parabolic-like band shape after each set of complementary turns grows quadratically. This is for the high-pure advection regime, where the effects of diffusion are negligible.

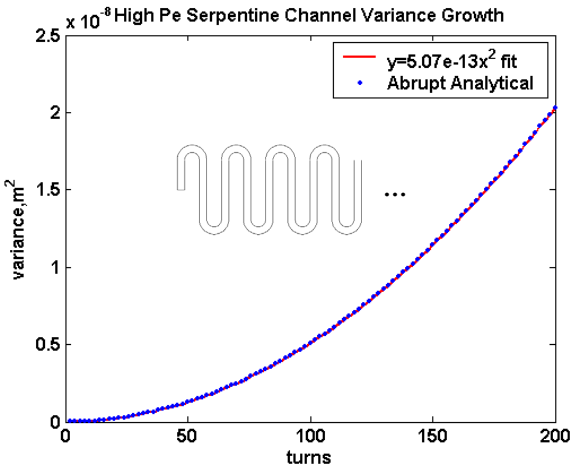

Figure 17 – Variance growth with increasing number of complementary turns in system. w/r_c=0.4, a=10μm.

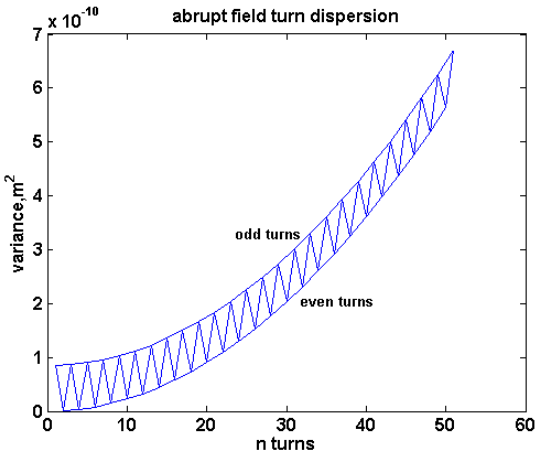

Figure 18 – Plot of the turn dispersion after even and odd turns for w/r_c=0.4. The top line represents the dispersion after only the odd numbered turns. The bottom line represents the dispersion after only the even numbered turns. The zig-zagging line represents the variance after both sets of turns.

The source of this quadratic growth is apparent in the expanded form of (30), seen in (a19) in the Appendix. Every term of (a19) contains an n^2, which indicates that the variance grows quadratically with both even- and odd-numbered turns. An example of this is shown in figure 18.

The variance grows quadratically for either even or odd sets of turns. However, when following the variance after both sets of turns, it alternates high and low, since the variance grows after odd turns and is subsequently reduced after even-complementary turns. Figure 18 makes it apparent why odd-turned designs are not practical, since they always produce more variance than an even-turned design.

In reality, since the system is limited in size, the variance cannot continue to grow to an arbitrarily large quantity. However, until a physical limit is reached, the growth rate, since quadratic, will be significantly large. Such effects will be discussed further in section 3.6. The variance results in figures 17 and 18 are all valid for high Peclet regimes (the high-pure advection region in figure 13). In the next section, diffusion will be considered to examine the pure advection (green) regime of figure 13, where many microfluidic designs lie [3,4]. Even with diffusion, super-linear growth rates for dispersion can be observed.

3.5 Particle Simulation Results with 0-Assumption Field Model

With the full Laplacian field structure, a direct first-principles derivation of a closed-form algebraic expression for the high-Peclet band dispersion is not possible using the analysis from the previous section due to the non-fully developed flow patterns created by the transition electric fields. So in this section, a particle simulator was created in Matlab, [13], using numerical solutions of the full Laplacian field equations, (15), to determine the dynamics of particles placed in the channel. These dynamics are described by the Helmholtz-Smoluchowski equation, re-written from (3) here:

$$\frac{d\vec{x}}{dt} = \mu\vec{E}\,, \tag{34}$$

where $\vec{x}$ is the position vector, μ is the species mobility, and $\vec{E}$ is the electric field, which can be represented by the full Laplacian solution, (15), or the abrupt-transition solution, (6).

The particle simulator is fed the geometry and physical properties of the system such as the inner and outer radii, *a* and *b*, the straight leg lengths, *L*, the number of curves, *n*, the particle mobility, μ, the applied electric potential, V_o, and the number of particles, *pts*. Then, the simulator numerically solves (34) to provide the particle trajectories. Figure 19 shows the geometry input for the simulator.

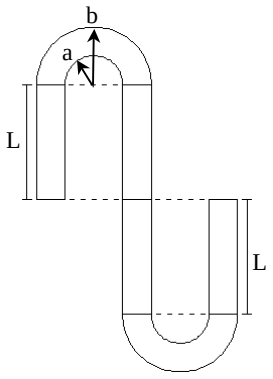

Figure 19 – Geometry input to the particle simulator.

After running the time necessary for the mean of the band to reach the defined end of the serpentine channel, the particle simulator produces an array of particle locations. Then, by using the

discretized form of (25), implemented through the Matlab *var()* function, the sample variance is calculated, which represents the variance of the band in the channel.

Now, the particle simulator will be used to verify the analytical abrupt-transition 1/*r* field variance. Then, simulation results can be generated for the full Laplacian transition field, and new comparisons can be made between the abrupt and Laplacian transition field variance predictions.

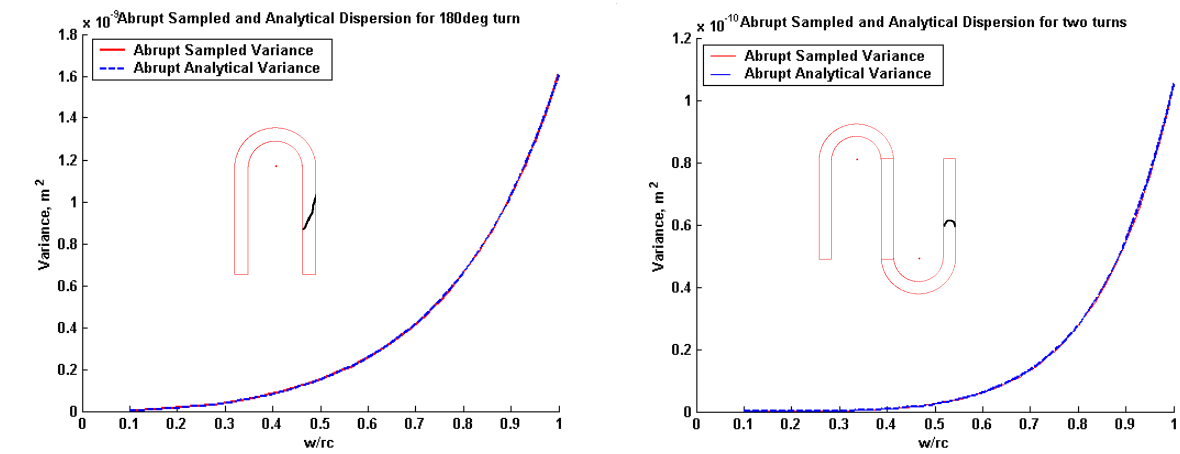

(a) (b)

Figure 20 – (a) Comparison of the abrupt-transition field particle simulation variance to the analytical expression of the variance for a single turn with w/r_c ranging from 0.1 to 1.0. (b) Comparison of the particle abrupt-transition field particle simulation variance to the analytical expression of the variance for complementary turns with w/r_c from 0.1 to 1.0. In both cases, agreement is excellent.

Figures 20a and 20b compare and verify the particle simulator's abrupt-transition 1/*r* field variance results to the analytical expressions from the previous section. Since w/r_c is the only non-dimensional variable for infinite-Peclet dispersion, which can be verified with the Buckingham π-Theorem in the Appendix, the first graph shows the results for a range of w/r_c values from 0.1 to 1.0, which more than encompasses the majority of the practical design space which lies in the range 0.1 to 0.4, as previously mentioned. From these figures, the analytical expressions from the previous section can be seen to be in excellent agreement with the particle simulator across the entire range of w/r_c, with the error consistently near the floor of the computer's precision.

Next, dispersion results for the full Laplacian transition fields can be generated for the same range of w/r_c values (0.1 to 1.0) and compared to the abrupt-transition field dispersion. Figure 21 shows the

results of a particle simulation at a single w/r_c value, 0.667, which runs with abrupt-transition (red) and full Laplacian transition (blue) electric fields. They are compared with the variance results from a linear (green) electric field in the curve, which comes from the expression $skew^2/12$.

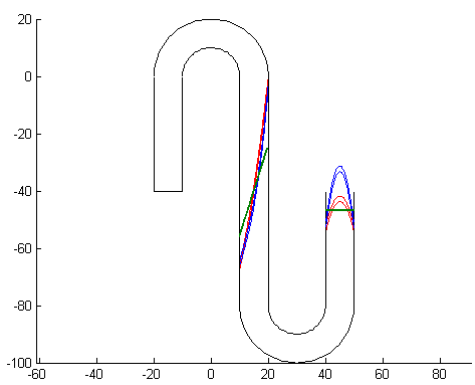

Figure 21 – Particle simulations traveling left to right for w/r_c=0.667 with the full Laplacian transition field (blue) and the abrupt-transition $1/r$ field (red) compared with the linear field approximation skew (green).

Figure 22a compares the abrupt-transition $1/r$ and Laplacian field variance results with the skew variance resulting from the 2-assumption linear field model for w/r_c ranging from 0.1 to 1.0 for a single turn. Figure 22b shows the two results compared with the 2-assumption linear field model for a set of complementary turns for the same w/r_c range. In figure 22a, the difference between the two descriptions is not that significant or that different from the linear field variance, $skew^2/12$, for small w/r_c. This region of w/r_c is where the error of the linear approximation for the field in the curve is becoming smaller, so the agreement of the three becomes fairly good. However, for complementary turns, even at low w/r_c the linear and $1/r$ abrupt-transition approximations miss vital contributions to the dispersion and therefore do not agree well with the full Laplacian transition electric field model.

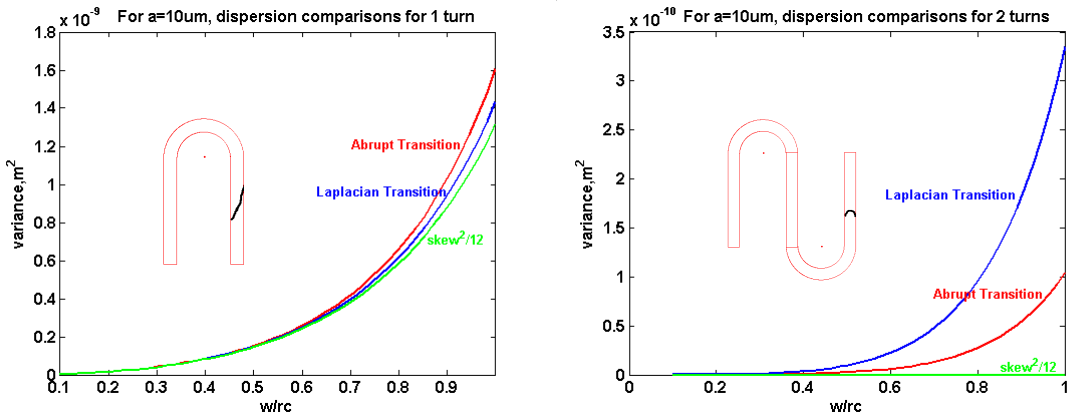

(a) (b)

Figure 22 – The figure on the left shows the resulting variance for single turn channels with a w/r_c from 0.1 to 1.0. The figure on the right shows the resulting variance for complementary turns for the same range of w/r_c.

In the previous section with abrupt-transition $1/r$ fields, a quadratic growth was discovered in the variance after traveling through n complementary sets of turns using the analytical equations for abrupt-transition field dispersion. Using the particle simulator, the same test can be run using the Laplacian transition fields. Figure 23a shows the results of a particle simulation for the abrupt-transition $1/r$ and Laplacian fields through three sets of complementary turns. The increase in band variance is apparent after each individual turn and particularly after each set of complementary turns. Even after the odd turns that come after at least one set of complementary turns, the mid-section of the band begins to outrun the edges, which occurs when the mid-section gets far enough ahead of the band edges so that not even the larger velocity of the inner radius particles is enough to catch up with the forward stretched mid-band particles. Figure 23b shows the results of this test for six complementary sets of turns, or twelve turns total. Again, quadratic growth is apparent. Of course, the linear field approximations would predict exactly zero variance after each set of complementary turns.

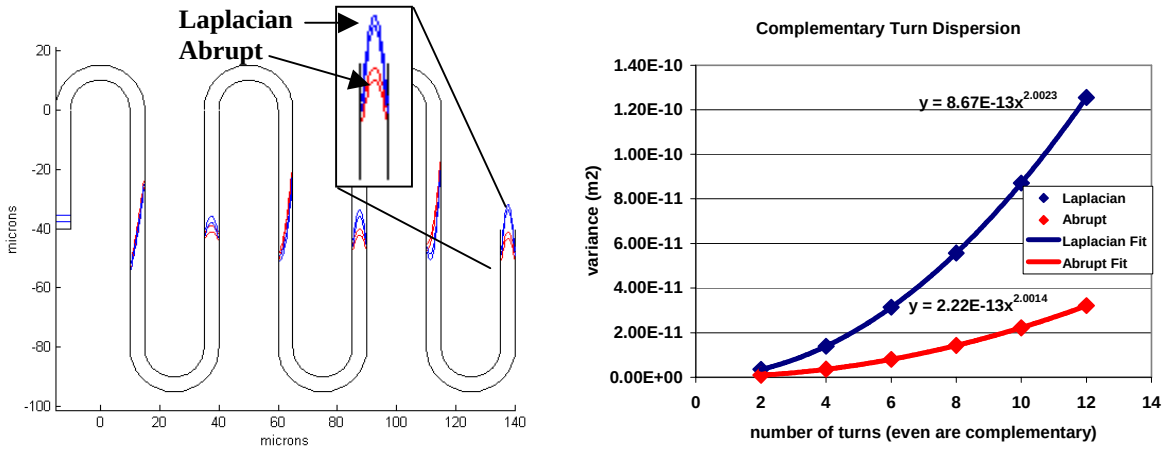

Figure 23 – (a) Three complementary turns simulated with the particle simulator for w/r_c=0.4. (b) Variance after multiple complementary turns for Laplacian and abrupt-transition 1/r fields, showing quadratic growth in both cases. w/r_c=0.4, a=10μm.

One observation from figure 23b is that since both Laplacian and abrupt-transition 1/r field variance descriptions have quadratic growth in this high-pure advection regime, they differ only by a constant, which in the case of figure 23b is slightly less than four. This fact will be used in section 3.7 to determine a relationship between analytical variance descriptions using the abrupt-transition electric field in (30) and the variance descriptions using the Laplacian electric field determined by the particle simulator in order to create a closed form analytical description of the Laplacian variance in the high-pure advection regime.

To validate some of the Laplacian particle simulation results and to extend them to include diffusion in the other three regimes, FEMLAB simulations will be shown in the next section.

3.6 Multi-Regime FEMLAB Validation Results

FEMLAB can be used to numerically solve the partial differential advection-diffusion equation and the electrostatic field structure necessary to solve the dynamics of a separation system [14]. In this section, FEMLAB will be used to provide validation results for the models shown in previous sections and self-validation compared to published experiments. The FEMLAB simulations involve an unsymmetric coupling, where the advection part of the advection-diffusion equation, (4), is coupled to the

electric field through the Helmholtz-Schmolochowski relation, (3), but according to the electroneutrality condition previously assumed, the species concentration has no effect on the electric field. FEMLAB can also be used to couple any number of custom-input equations. Using this feature, FEMLAB can be used to verify the abrupt-transition field results as well.

The first simulation run with FEMLAB is a complementary turn, with w/r_c=0.4, in the high-pure advection regime that compares to the particle simulations for abrupt-transition and Laplacian fields.

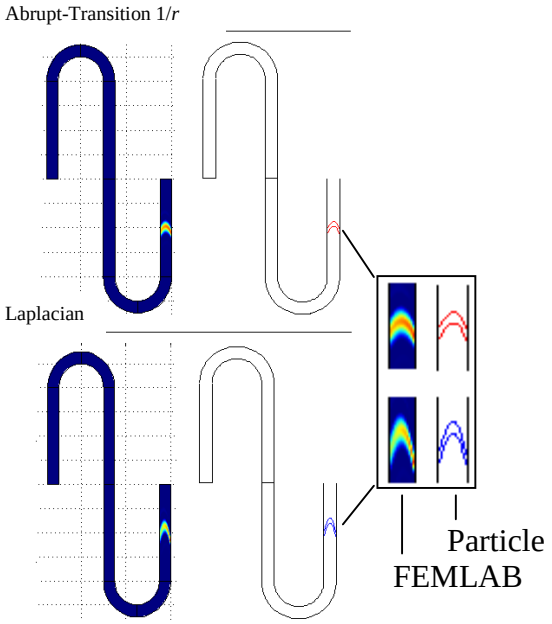

Figure 24 – FEMLAB validation of abrupt-transition and Laplacian field particle simulations, where FEMLAB used a diffusion coefficient of zero. This simulation uses a center radius, r_c=12.5μm, length between turns, L_{bt}=80μm, mobility, μ=1.5·10^{-7}m^2/Vs, straight leg electric field, E_y=8420.17V/m, and diffusivity, D=0.

Figure 24 shows this validation by using a diffusion coefficient of zero to obtain an infinite Peclet number, or as close to infinite as the solver tolerances allow. The FEMLAB simulation confirms the different shapes after a set of complementary turns, indicating that the Laplacian fields provide a significant increase in variance over the simpler abrupt-transition fields, and an infinite increase compared to the linear fields, which would completely unskew the band. The spreading of the band apparent in the FEMLAB figures is a result of the initial Gaussian band that was injected into the channels, in contrast to the uniform initial band that is implicit in the particle simulation.

Now to compare FEMLAB with experimental results, a simulation can be run that replicates the system in Ramsey's experiment in [4]. This involves measuring the dispersion as the band moves through the channel, excluding the curved sections. The system has an r_c=125μm, a w=60μm, an L_{bt}=6mm, an average electric field intensity of 60V/cm, a mobility of $1.195 \cdot 10^{-8}$ m^2/Vs, and a Peclet number of 138. The geometry is shown in figure 25a, and the results of the simulation are shown in figure 25b.

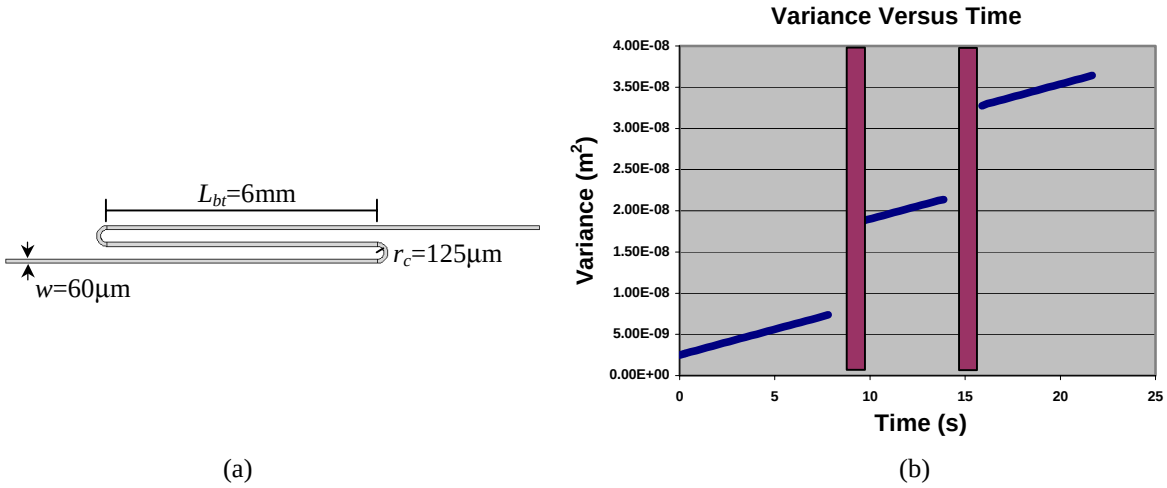

(a) (b)

Figure 25 – (a) The geometry corresponding to Ramsey's experiment in [4]. (b) FEMLAB simulation of a separation based on Ramsey's experiment using the geometry in figure 25a for a Pe=138.

The slope of the lines in figure 25b corresponds to 2D, where D is the diffusion coefficient and 2D is the rate of variance growth, and the jumps after the curves, represented by the vertical bars, are the variance added due to the turn. The slope results in a diffusion coefficient of $3.12 \cdot 10^{-10} m^2/s$ and the jumps in the plot correspond to turn-induced variance of $1.01 \cdot 10^{-8} m^2$, both of which are in good agreement with Ramsey's experimental results.

Finally, FEMLAB can be used to verify the quadratic variance growth seen with both abrupt-transition 1/r and Laplacian fields by using the geometry shown in figure 26a with an increasing Peclet number. The results in figure 26b are for Peclet numbers ranging from 500 to 10,000, where the diffusion coefficient was varied while the geometry was held constant.

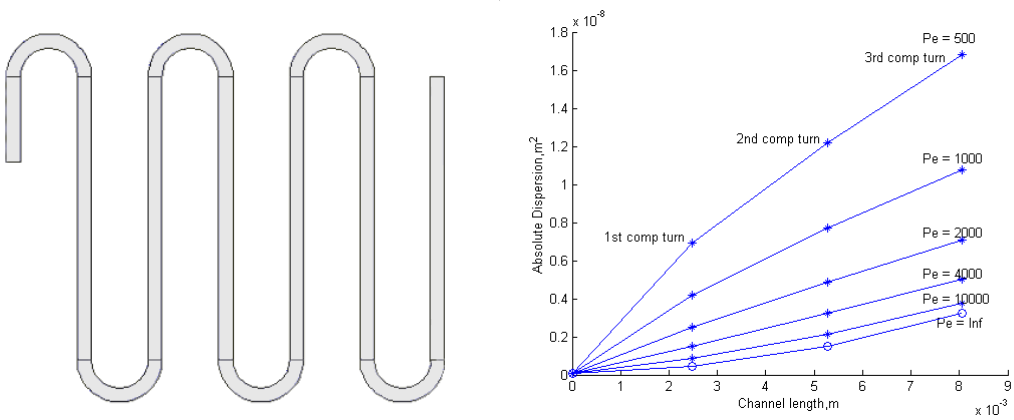

(a) (b)

Figure 26 – (a) Geometry for FEMLAB results in figure 26b. w=50μm, r_c=125μm, L_{bt}=1000μm. (b) FEMLAB variance results for the multi-turn channel geometry in figure 26a for Pe=500 to 10,000.

Figure 26b shows the growth rate approaching the quadratic infinite Peclet growth as the Peclet number is increased. It also shows the effects of the other regimes on the growth rate, where diffusion is more prevalent. As diffusion is increased, it shows the movement from the high Peclet super-linear to lower Peclet linear and sub-linear growth. While the high Peclet super-linear growth is well understood to be due to the quadratic dependence on the number of turns traversed, as seen in (a19) and (a24) in the Appendix, the reason for the trend to sub-linear growth is not as apparent. This trend in the growth rate involves the interaction of field and geometry based dispersion, axial diffusion, and transverse diffusion, which all interact differently as the Peclet number is changed. At first, this transition from super-linear to sub-linear might be from the measurement limitations mentioned in section 3.4. However this is not the case. Such measurement limitations come from the fact that it is impossible for the variance to grow beyond the square of the length of the straight section where the band variance is measured. However, in this case the late-time asymptote of such a limitation in the measurement is at $1 \cdot 10^{-6}$ m^2, which is several orders of magnitude above the current set of results, and is therefore not limiting the growth of the variance measurements. It is interesting to note, however, that all regimes will eventually approach the late-time asymptote, and it is something that should not be ignored when making such measurements.

3.7 High-Pure Advection Analytical Dispersion with 0-Assumption Field Model

In this section, some of the results gathered from the analytical abrupt-transition $1/r$ field variance and particle model Laplacian field variance simulations in the previous section will be used to obtain a high-Peclet analytical description with the full Laplacian transition field structure.

Since a first-principles derivation is not possible to develop the analytical expression for the full Laplacian field variance, the relationship between the abrupt-transition and Laplacian field variances needs to be characterized. From this characterization a relational factor dependent on the problem space can be defined to correct the abrupt-transition field analytical variance descriptions to form a complete Laplacian analytical description of the band variance.

From section 3.5 it is known that there is a constant factor between the two descriptions for any number of turns for a given w/r_c. So, the only thing that needs to be characterized is the factor between the two expressions for a w/r_c range for even- and odd-numbered turns. To do this, a series of particle simulations were run to determine the Laplacian variance results, which were then compared with the analytical expression for the abrupt-transition field variance. The factors for even- and odd- numbered turns are shown in Figures 27a and 27b.

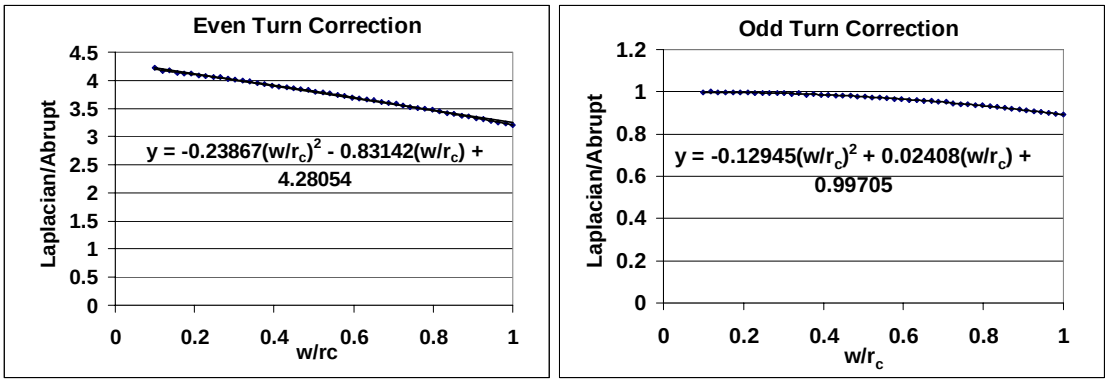

(a) (b)

Figure 27 – Correction factors for the abrupt-transition field variance equations in (30) for even-numbered turns, (a), and odd-numbered turns, (b).

Using the correction factors in figure 27, which are weak functions of w/r_c, a new expression for the variance using the Laplacian transition field structure can be created, and this is shown here with an expanded version in the Appendix:

$$\sigma_{lap}^2 = \lambda \frac{\pi^2 \ln^2(b/a)}{w^3} \int_a^b \left(N_1 r^2 + N_2 (w + 2a - r)^2 - \frac{(N_1 + N_2)((w+a)^3 - a^3)}{3w} \right)^2 dr, \quad (35)$$

where

$$\lambda = \alpha \left(\frac{w}{r_c} \right)^2 + \beta \left(\frac{w}{r_c} \right) + \gamma, \quad (36)$$

$$\alpha = \text{mod}(n,2)(-0.12945) + (1 - \text{mod}(n,2))(-0.23867), \quad (37)$$

$$\beta = \text{mod}(n,2)(0.02408) + (1 - \text{mod}(n,2))(-0.83142), \quad (38)$$

$$\gamma = \text{mod}(n,2)(0.99705) + (1 - \text{mod}(n,2))(4.28054) \quad (39)$$

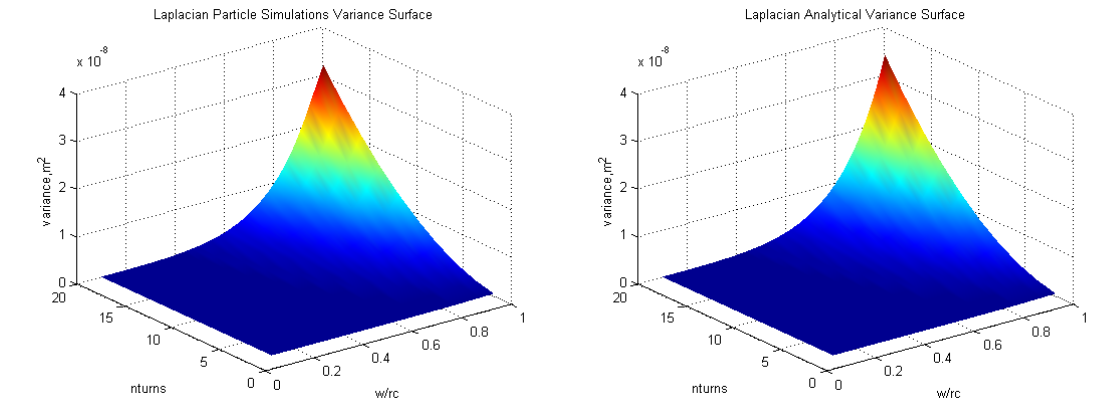

(a) (b)

Figure 28 – A surface representing the variance of a band after traveling through a channel, with w/r_c ranging from 0.1 to1.0 and n ranging even numbered from 2 to 20, as described by the particle simulation in (a) and (35) in (b).

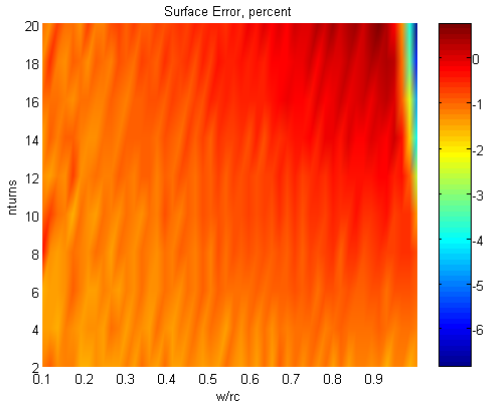

Figure 29 – The error between the two surfaces seen in figure 28.

To verify the new expression in (35), a surface was created over a parameter space consisting of w/r_c and the number of turns using the particle simulator. The number of turns is the even-numbered turns up to 20 and w/r_c ranges from 0.1 to 1.0, a superset of the typical w/r_c design space for serpentine channels which goes up to 0.4. The surfaces are seen in figure 28 and the error between the two is illustrated in figure 29.

The error in figure 29 is computed from the difference of the two surfaces normalized by the surface described by the particle simulation. Over nearly the entire surface, the error remains less than 1%. Only in the corner defined by w/r_c values near 1.0 does the error begin to increase to approximately 6%. The source of this slightly increasing inaccuracy remains to be investigated. However, since this is an area of the parameter space that would rarely, if ever, be used for useful designs, the error has no real effect on the performance of the model. Further, since the assumptions appear to hold for the entire feasible design space, w/r_c equals 0.1 to 0.4, the performance is considered acceptable. If needed, the error could be removed by renormalizing the analytical variance surface.

4. Conclusion

This report has presented a new model of the high Peclet variance from the electric field and channel geometry using the full structure of the electric fields described by complete solutions to Laplace's equation. This is a functional form, as described in [6], that can be used as a component model in a separation system when combined with other subsystems such as the injector and detector. As a closed-form algebraic expression this model can be used for rapid computation and gradient-based optimization.

To create this model, this report first presented additional solutions to the field structure in the serpentine turns, which gradually relaxed the two main assumptions of linear fields in the curves with an abrupt transition to the straight sections made in [2,3,4,5]. The first field solution presented in chapter 2, removed the assumption of linear field structure using a $1/r$ field in the curves while still using an abrupt transition to the straight sections. The second field solution presented in chapter 2 used complete solutions to Laplace's equation to have a continuous transition between sections with the correct structure in straight and curved sections, as verified with finite element software. In chapter 3, an analytical model of the variance of a band traveling through the serpentine channels was created using the abrupt-transition $1/r$ 1-assumption field structure. Using this variance model, new effects were predicted, such as incomplete unskewing after complementary turns and quadratic growth of the variance after n even or odd turns, which were confirmed in FEMLAB simulations. Finally, this abrupt-transition model was combined with results from the Matlab particle simulations using the 0-assumption full Laplacian field structure to create the complete high Peclet variance model.

4.1 Future Work

In its current functional form, the high Peclet variance model will be combined with the method of moments, M.O.M., model developed at CMU [to be published] to describe the variance produced by a serpentine of any number of turns in any regime of figure 13. Ultimately, the variance descriptions and insight gained from the high Peclet variance expressions in this work will be used to create a component

based model for serpentine channels, which will be useful for creating any general serpentine geometry with uniform width. This component model will be only for the turns in serpentine channels combined with the straight section model of the M.O.M., which will allow general serpentines to be constructed piece by piece. The challenge in converting the functional variance descriptions in this report will be modifying them to accept various initial conditions, since the input to the component model will be the output of the previous straight section after an arbitrary number of turns, rather than a well-defined injector.

Appendix

A.1 Buckingham π-Theorem

Background: See Harald Hanche-Olsen's notes in [15] for further details. Provided below are a partial proof and examples of the Buckingham π-Theorem from previous sections of this report:

Assuming variables with values and units that describe a physical function, $\Phi(R_1,\ldots,R_n)$, according to the following notation:

$$R_j = v(R_j)[R_j], \tag{a5}$$

where R_j is the variable with value $v(R_j)$ and units $[R_j]$

Further, it is assumed the units of the variable(s) can be broken down into fundamental units such as m, kg, s, K, using a consistent set such as MKS. These units can be represented as $F_1,\ldots,F_m$. This allows representation of the units of the variable(s) as a product of powers:

$$[R_j] = \prod_{i=1}^{m} F_i^{a_{ij}} \qquad (j = 1,..,n), \tag{a6}$$

where it is necessary that the units themselves are independent such that:

$$\prod_{i=1}^{m} F_i^{x_i} = 1 \qquad (x_1 = .. = x_m = 0) \tag{a7}$$

Now a matrix of the powers in the product series is constructed, whose dimensions depend on the number of variables, n, and the number of fundamental units used, m.

$$A = \begin{bmatrix} a_{11} & \cdots & a_{1n} \\ \vdots & \ddots & \vdots \\ a_{m1} & \cdots & a_{mn} \end{bmatrix} \tag{a8}$$

Using these properties we can define a non-dimensional group from the original variables. Such a group is constructed out of a series of products of the original variables of the system, R_j, raised to the necessary powers, λ_n. Such a group would have units defined as:

$$[R_1^{\lambda_1} \cdots R_n^{\lambda_n}] = \prod_{i=1}^{m} F_i^{a_{i1}\lambda_1 + \cdots + a_{in}\lambda_n} \tag{a9}$$

For this group of units to be dimensionless, or for (a9) to equal one, the power of the product series must equal zero, which is equivalent to $A\lambda=0$, where $\lambda=[\lambda_1,\ldots,\lambda_n]^T$. Therefore, finding the null-space of A, $N(A)$, will provide the set of powers necessary to have a set of non-dimensional variables. It can provide the maximal set of non-dimensional variables $[\pi_1,\ldots,\pi_{n-r(A)}]$ without knowledge of the underlying physical equations that are the source of the dimensional analysis. $r(A)$ is the rank of A, therefore, n-$r(A)$ is the number of free variables, which set the number of independent vectors in the null space of A for our under-specified linear system. The vectors that compose $N(A)$ then define the form of the non-dimensional variables.

Example 1 (from section 3.1)

An example, based on the non-dimensionalization of the function describing the variance of a band traveling through serpentine channels in any of the four regimes shown in figure 13 begins with the function describing the variance:

$$\Phi(w, r_c, l_{bt}, E_c, D, \mu) \tag{a10}$$

where w is the channel width, r_c is the center radius of the turn, L_{bt} is the length between turns, E_c is the constant field strength in the straight sections, D is the diffusion coefficient, and μ is the mobility of the separation species. Each of these variables, R_j, contributes to the set of fundamental units F_i, to create the set of $F=\{m,kg,s,A\}$. This allows the matrix of variable unit powers A to be constructed:

$$A=\begin{bmatrix} 1 & 1 & 1 & 1 & 2 & 0 \\ 0 & 0 & 0 & 1 & 0 & -1 \\ 0 & 0 & 0 & -3 & -1 & 2 \\ 0 & 0 & 0 & -1 & 0 & 1 \end{bmatrix}, \tag{a11}$$

where the columns represent variables, $[w,r_c,L_{bt},E_c,D,\mu]$, and the rows represent fundamental units, $[m,kg,s,A]^T$.

Finding the nullspace of A, $N(A)$ provides the following result:

$$N(A)=\begin{bmatrix} -1 & -1 & 1 \\ 1 & 0 & 0 \\ 0 & 1 & 0 \\ 0 & 0 & 1 \\ 0 & 0 & -1 \\ 0 & 0 & 1 \end{bmatrix} \tag{a12}$$

The powers of the variables in each of the non-dimensional groups are represented in the chosen basis of $N(A)$. For this example, the three non-dimensional groups are therefore:

$$\pi=\begin{bmatrix} \frac{r_c}{w} & \frac{l_{bt}}{w} & \frac{\mu E_c w}{D} \end{bmatrix} \tag{a13}$$

Example 2 (from Section 3.5)

Following the same procedure for the analysis of high-pure advection regime results in the following trivial example:

$$\Phi(w, r_c), \tag{a14}$$

where the triviality lies in the fact that there are no time-dependent parameters, since diffusion is not an issue. Therefore the variance fundamentally only depends on w and r_c. This gives the following results for the non-dimensional parameters of which there will be one, n-$r(A)$=1:

$$A=\begin{bmatrix} 1 & 1 \end{bmatrix} \tag{a15}$$

$$N(A)=\begin{bmatrix} -1 \\ 1 \end{bmatrix} \tag{a16}$$

$$\pi=\begin{bmatrix} \frac{r_c}{w} \end{bmatrix} \tag{a17}$$

A.2 Expanded Algebraic Form of Equation 30.

Expanding Equation 30 from the text, repeated here:

$$\sigma_{ab}^2=\frac{\pi^2 \ln^2(b/a)}{w^3}\int_a^b\left(N_1 r^2+N_2(w+2a-r)^2-\frac{(N_1+N_2)((w+a)^3-a^3)}{3w}\right)^2 dr \tag{a18}$$

creates the following closed form algebraic for the high-pure advection variance using the abrupt 1/*r* fields in the turns:

$$\sigma_{ab}^2 = \frac{\pi^2 \ln^2(b/a)}{15w^2}\begin{pmatrix} 15G^2 + 15a^4(N_1+N_2)^2 + 30a^3w(N_1+N_2)^2 + \\ 10a^2w^2(3N_1^{\,2} + 4N_1N_2 + 3N_2^{\,2}) + 5aw^3(3N_1^{\,2} + 2N_1N_2 + 3N_2^{\,2}) + \\ w^4(3N_1^{\,2} + N_1N_2 + 3N_2^{\,2}) - 10G(N_1+N_2)(3a^2 + 3aw + w^2) \end{pmatrix}, \quad \text{(a19)}$$

where

$$G = \frac{1}{3w}(N_1+N_2)((w+a)^3 - a^3) \quad \text{(a20)}$$

$$N_1 = \frac{n + \mathrm{mod}(n,2)}{2} \quad \text{(a21)}$$

$$N_2 = \frac{n + \mathrm{mod}(n+1,2) - 1}{2} \quad \text{(a22)}$$

A.3 Expanded Algebraic Form of Equation 35.

The expanded form of 35 is identical to (a19) except for the correction factor in (36), which results in the following:

$$\sigma_{lap}^2 = \lambda \frac{\pi^2 \ln^2(b/a)}{w^3} \int_a^b \left(N_1 r^2 + N_2(w + 2a - r)^2 - \frac{(N_1+N_2)((w+a)^3 - a^3)}{3w} \right)^2 dr \quad \text{(a23)}$$

$$\sigma_{lap}^2 = \lambda \frac{\pi^2 \ln^2(b/a)}{15w^2}\begin{pmatrix} 15G^2 + 15a^4(N_1+N_2)^2 + 30a^3w(N_1+N_2)^2 + \\ 10a^2w^2(3N_1^{\,2} + 4N_1N_2 + 3N_2^{\,2}) + 5aw^3(3N_1^{\,2} + 2N_1N_2 + 3N_2^{\,2}) + \\ w^4(3N_1^{\,2} + N_1N_2 + 3N_2^{\,2}) - 10G(N_1+N_2)(3a^2 + 3aw + w^2) \end{pmatrix}, \quad \text{(a24)}$$

where G, N_1, and N_2 are the same as in (a20), (a21), and (a22) respectively, and from (36), (37), (38), and (39):

$$\lambda = \alpha\left(\frac{w}{r_c}\right)^2 + \beta\left(\frac{w}{r_c}\right) + \gamma, \quad \text{(a25)}$$

$$\alpha = \mathrm{mod}(n,2)(-0.12945) + (1 - \mathrm{mod}(n,2))(-0.23867), \quad \text{(a26)}$$

$$\beta = \mathrm{mod}(n,2)(0.02408) + (1 - \mathrm{mod}(n,2))(-0.83142), \quad \text{(a27)}$$

$$\gamma = \mathrm{mod}(n,2)(0.99705) + (1 - \mathrm{mod}(n,2))(4.28054) \quad \text{(a28)}$$

References

[1] Manz, A., Harrison, D.J., Verpoorte, E., Widmer, H.M., Vol. 33, *Advanced Chromatography* 1993, pp. 1-66.

[2] Griffiths, S.K., Nilson, R.H., Vol. 73, *Analytical Chemistry* 2001, pp. 272-278.

[3] Molho, J.I., Herr, A.E., Mosier, B.P., Santiago, J.G., Kenny, T.W., et.al., Vol. 73, *Analytical Chemistry* 2001, pp. 1350-1360.

[4] Culbertson, C.T., Jacobson, S.C., Ramsey, M.J., Vol. 70, *Analytical Chemistry* 1998, pp. 3781-3789.

[5] Griffiths, S.K., Nilson, R.H., Vol. 72, *Analytical Chemistry* 2000, pp. 5473-5482.

[6] Mukherjee, T., Fedder, G.K., Ramaswamy, D., White, J., Vol. 19, Issue 12, *IEEE Transactions on Computer Aided Design of Integrated Circuits and Systems*, pp. 1572-1589.

[7] Paegel, B.M., Lester, D.H., Simpson, P.C., Mathies, R.A., Vol. 72, *Analytical Chemistry* 2000, pp. 3030-3037.

[8] Probstein, R.F. *Physicochemical Hydrodynamics: An Introduction*, 2nd ed.; John Wiley & Sons: New York, 1994

[9] Melcher, J.R. *Continuum Electromechanics*; The MIT Press: Cambridge, Massachussetts, 1981.

[10] Hunter, J.H. *Zeta Potential in Colloid Science: Principles and Applications*, Academic Press: New York, 1981.

[11] Sternberg, J.C., Vol. 2, *Advances in Chromatography*, Giddings, J.C., Keller, R.A., Editors, Marcel Dekker: New York, 1966, pp. 205-270.

[12] Bharadwaj, R., Santiago, J.G., Mohammadi, B., Vol. 23, *Electrophoresis* 2002, pp. 2729-2744.

[13] Matlab web page, *http://www.mathworks.com*, The Mathworks, Inc.

[14] FEMLAB web page, *http://www.comsol.com*, Comsol, Inc.

[15] Hanche-Olsen, H., "Buckingham's π-Theorem", http://www.math.ntnu.no/~hanche/notes/buckingham/buckingham-a4.pdf. 1998.

[16] Zahn, M. *Electromagnetic Field Theory: a problem solving approach*, Wiley and Sons: New York, 1979.

Symbol Glossary

a	inner turn radius
b	outer turn radius
c	concentration
c_{avg}	average concentration
C_n	series coefficients for the Laplacian solutions in the curved sections
D	diffusion
D_n	series coefficients for the Laplacian solutions in the straight sections
E_x^{curve}	transverse electric field component in the straight section (Laplacian transition field)
E_y	axial electric field component in the straight section (abrupt-transition 1/r field)
$E_y^{straight}$	axial electric field component in the straight section (Laplacian transition field)
E_r^{curve}	radial electric field component in the curved section (Laplacian transition field)
E_ϕ	circumferential electric field component in the curved section (abrupt-transition 1/r field)
E_ϕ^{curve}	circumferential electric field component in the curved section (Laplacian transition field)
G	common factor found in the abrupt and Laplacian analytical variance equations
k	Boltzmann's constant
k	wave number in the Laplacian series solutions
l	straight channel length for uniform symmetric single turns
L_{bt}	length between turns for serpentine channels
L_{det}	length of the last leg of serpentine going to the detector
L_{inj}	length of first leg of serpentine coming from the injector
n	number of turns in the serpentine channel
$n_\pm$	ion concentration in the double layer for positive(+) and negative(-) ions
$n_\pm^o$	ion concentration in the bulk for positive(+) or negative(-) ions
N_1	indexing modulo function for odd turns found in analytical variance expressions
N_2	indexing modulo function for even turns found in analytical variance expressions
Pe	Peclet number based on width
pts	number of particles in the Matlab particle simulation
q_e	charge of an electron
r	radial position in the curved section of the channels
r_c	mean channel width
$skew$	the skew of a band traveling in a linear electric field in a turn
t	time
T	temperature
T_{bt}	travel time ratio of width to length between turns
T_i	time for a particle to travel the inner most radius in the turn
T_o	time for a particle to travel the outer most radius in the turn
T_t	travel time ratio of width to length of turn along center radius
$\vec{u}$	channel velocity field
u_o	mean channel velocity
V_o	applied electric potential
w	channel width
x	transverse direction in the straight section of the channels
y	axial direction in the straight section of the channels
z	ion valency
α	component of the correction factor λ
β	component of the correction factor λ
ε	buffer permittivity
Φ	electric potential

ϕ angular position in the curved section of the channels
γ component of the correction factor λ
η Laplacian series, coefficient coupling block matrix component
λ correction factor for the abrupt analytical variance to produce the Laplacian analytical variance
μ species mobility
μ_v viscosity of the buffer
θ turn angle
ρ free-charge density
σ_{ab}^2 abrupt-transition $1/r$ field analytical variance
σ_{lap}^2 full Laplacian transition field analytical variance
τ Laplacian series, coefficient coupling block matrix component
ξ Laplacian series, coefficient coupling block matrix component
ζ zeta potential

Normalized Variables

c^* concentration, $c^*=c/c_o$
t^* time, $t^*=t/(w/u_o)$
u^* velocity, $u^*=\bar{u}/u_o$
x^* transverse position, $x^*=x/w$
y^* axial position, $y^*=y/w$

Acknowledgements

All of my MEMS and SYNBIOSYS group members deserve many thanks for their help and involvement with my work as a master's student. In particular my two advisors, Dr. Hoburg and Dr. Mukherjee, deserve thanks for their insightful comments, discussions, and advice. Also, I would like to thank Dr. Hauan for the use of his Beowulf cluster to run my many simulations. I am grateful to Mary Moore for her very helpful proofreading advice, and my friends and family for all of their support.

This research effort was sponsored by the Defense Advanced Research Projects Agency under the Air Force Research Laboratory, Air Force Material Command, USAF, under grant number F30602-01-2-0587.